Variable physical drivers of near-surface turbulence in a regulated river

Sofya Guseva[1], Mika Aurela[2], Alicia Cortes[3], Rigel Kivi[2], Eliisa Selina Lotsari[4], Sally Macintyre[3], Ivan Mammarella[5], Anne Ojala[5], Victor M Stepanenko[6], Petteri Uotila[5], Aki Vähä[5], Timo Vesala[7], Marcus B. Wallin[8], and Andreas Lorke[9]

[1]University Koblenz-Landau (Landau)
[2]Finnish Meteorological Institute
[3]University of California, Santa Barbara
[4]University of Eastern Finland
[5]University of Helsinki
[6]Lomonosov Moscow State University
[7]University of Helsinki, Institute for Atmospheric and Earth System Research
[8]Swedish University of Agricultural Sciences
[9]University of Koblenz and Landau

November 23, 2022

Abstract

Inland waters, such as lakes, reservoirs and rivers, are important sources of greenhouse gases to the atmosphere. A key parameter that regulates the gas exchange between water and the atmosphere is the gas transfer velocity, which itself is controlled by near-surface turbulence in the water. While in lakes and reservoirs, near-surface turbulence is mainly driven by atmospheric forcing, in shallow rivers and streams it is generated by flow-induced bottom friction. Large rivers represent a transition between these two cases. Near-surface turbulence has rarely been observed in rivers and the drivers of turbulence have not been quantified. We obtained continuous measurements of flow velocity and fluctuations from which we quantified turbulence, as the rate of dissipation of turbulent kinetic energy (ε) over the ice-free season in a large regulated river in Northern Finland. Atmospheric forcing was observed simultaneously. Measured values of ε were well predicted from bulk parameters, including mean flow velocity, wind speed, surface heat flux and a one-dimensional numerical turbulence model. Values ranged from $\sim 10^{-9}$ m^2 s^{-3} to 10^{-5} m^2 s^{-3}. Atmospheric forcing and river flow contributed to near-surface turbulence a similar fraction of the time, with variability in near-surface dissipation rate occurring at diel time scales, when the flow velocity was strongly affected by downstream dam operation. By combining scaling relations for boundary-layer turbulence at the river bed and at the air-water interface, we derived a simple model for estimating the relative contributions of wind speed and bottom friction in rivers as a function of flow depth.

Variable physical drivers of near-surface turbulence in a regulated river

S. Guseva[1], M. Aurela[2], A. Cortés[3], R. Kivi[4], E. Lotsari[5,6], S. MacIntyre[3], I. Mammarella[7], A. Ojala[8,9,10], V. Stepanenko[11,12], P. Uotila[7], A. Vähä[7], T. Vesala[7,9], M. B. Wallin[13,14] and A. Lorke[1]

[1]Institute for Environmental Sciences, University of Koblenz-Landau, Landau, Germany
[2]Climate Research Programme, Finnish Meteorological Institute, Helsinki, Finland
[3]Earth Research Institute, University of California, Santa Barbara, California
[4]Space and Earth Observation Centre, Finnish Meteorological Institute, Sodankylä, Finland
[5]Department of Geographical and Historical Studies, University of Eastern Finland, Joensuu, Finland
[6]Department of Geography and Geology, University of Turku, Turku, Finland
[7]Institute of Atmospheric and Earth System Research (INAR)/ Physics, University of Helsinki, Helsinki, Finland
[8]Ecosystems and Environment Research Programme, Faculty of Biological and Environmental Sciences, University of Helsinki, Helsinki, Finland
[9]Institute for Atmosphere and Earth System Research/Forest Sciences, Faculty of Agriculture and Forestry, University of Helsinki, Helsinki, Finland
[10]Helsinki Institute of Sustainability Science (HELSUS), Faculty of Biological and Environmental Sciences University of Helsinki, Helsinki, Finland
[11]Laboratory for Supercomputer Modeling of Climate System Processes, Research Computing Center, Lomonosov Moscow State University, Moscow, Russia
[12]Department of Meteorology and Climatology, Faculty of Geography, Lomonosov Moscow State University, Moscow, Russia
[13]Department of Earth Sciences: Air, Water and Landscape, Uppsala University, Uppsala, Sweden
[14]Department of Aquatic Sciences and Assessment, Swedish University of Agricultural Sciences, Uppsala, Sweden

Key Points:

- Atmospheric forcing and bottom friction make comparable contributions to near-surface turbulence in a regulated river
- Diel variability in dissipation rates of turbulent kinetic energy occur in response to flow regulation and wind forcing
- Scaling dissipation rates as a function of wind speed and flow velocity provides good agreement with observations

Corresponding author: Sofya Guseva, `guseva@uni-landau.de`

Abstract

Inland waters, such as lakes, reservoirs and rivers, are important sources of greenhouse gases to the atmosphere. A key parameter that regulates the gas exchange between water and the atmosphere is the gas transfer velocity, which itself is controlled by near-surface turbulence in the water. While in lakes and reservoirs, near-surface turbulence is mainly driven by atmospheric forcing, in shallow rivers and streams it is generated by flow-induced bottom friction. Large rivers represent a transition between these two cases. Near-surface turbulence has rarely been observed in rivers and the drivers of turbulence have not been quantified. We obtained continuous measurements of flow velocity and fluctuations from which we quantified turbulence, as the rate of dissipation of turbulent kinetic energy (ε) over the ice-free season in a large regulated river in Northern Finland. Atmospheric forcing was observed simultaneously. Measured values of ε were well predicted from bulk parameters, including mean flow velocity, wind speed, surface heat flux and a one-dimensional numerical turbulence model. Values ranged from $\sim 10^{-9}$ m^2 s^{-3} to 10^{-5} m^2 s^{-3}. Atmospheric forcing and river flow contributed to near-surface turbulence a similar fraction of the time, with variability in near-surface dissipation rate occurring at diel time scales, when the flow velocity was strongly affected by downstream dam operation. By combining scaling relations for boundary-layer turbulence at the river bed and at the air-water interface, we derived a simple model for estimating the relative contributions of wind speed and bottom friction in rivers as a function of flow depth.

Plain Language Summary

Inland water bodies such as lakes, reservoirs and rivers are an important source of greenhouse gases to the atmosphere. Gas exchange between water and the atmosphere is regulated by the gas transfer velocity and the difference in concentration between the mixed water layer and water surface. Considerable effort went into understanding the controls on gas transfer velocity, and it was revealed to depend on near-surface turbulence. Controls on large rivers are not yet understood as their surface area is sufficient for meteorological forcing to cause turbulence, as in lakes and reservoirs, yet some are shallow enough for currents to induce near bottom turbulence which propagates upwards. Here we quantify near-surface turbulence using data from continuous air and water side measurements, conducted over the ice-free season in a large subarctic regulated river in Finland. We find that turbulence, quantified as the dissipation rate of turbulent kinetic energy, is well described using equations for predicting turbulence from meteorological data for sufficiently high wind speeds and flow velocities. A new one-dimensional river model successfully captured these processes. Finally, we provide a simple model for estimating the relative contributions of the atmosphere and bottom friction as a function of depth.

1 Introduction

Inland waters produce, receive, transport and process organic and inorganic carbon and, relative to their surface area, are disproportionately important to regional and global carbon cycling (Cole et al., 2007; Tranvik et al., 2009; Aufdenkampe et al., 2011). River systems are often supersaturated in carbon dioxide (CO_2) and methane (CH_4), and release these radiatively-active gases to the atmosphere (Richey et al., 2002; Raymond et al., 2013; Borges et al., 2015). These gases are derived from terrestrial carbon sources and from organic carbon fixed in aquatic ecosystems, and the relative importance of these sources and their response to anthropogenic disturbance remain uncertain in most systems (Alin et al., 2011; Butman & Raymond, 2011).

A key parameter which regulates the gas exchange across the air-water interface is the gas transfer velocity (k), which is mainly controlled by turbulence on the water side of the interface. Both surface renewal and thin-film theories result in a dependence of the gas transfer velocity on the dissipation rate of turbulent kinetic energy near the water surface (Lamont & Scott, 1970; Zappa et al., 2007; Katul & Liu, 2017). Several mechanisms can contribute to the generation of turbulence in the surface boundary layer (SBL). In lentic aquatic systems, such as lakes and reservoirs, near-surface turbulence is mainly driven by atmospheric forcing, including wind shear, convective cooling and surface wave breaking (MacIntyre et al., 2010). Turbulence generation by wind shear can be described by boundary layer theory and energy dissipation rates scale with wind speed, while decreasing with increasing distance from the water surface (Wüest & Lorke, 2003; Tedford et al., 2014). In the open ocean, there is an increasing contribution of breaking surface waves to near-surface turbulence at wind speeds exceeding 6 m s^{-1} (Brumer et al., 2017). Convective mixing may occur if the net heat flux across the air-water interface is negative, and under such conditions, dissipation rates of turbulent kinetic energy scale with the surface buoyancy flux (Bouffard & Wüest, 2019). In shallow lotic ecosystems, such as streams, turbulence is mainly generated by bed friction and dissipation rates of turbulent kinetic energy scale with the mean flow velocity and decrease with increasing distance from the bed (Lorke & MacIntyre, 2009). Alin et al. (2011) suggested a conceptual scheme, in which the physical control of the gas transfer velocity in rivers undergoes a transition from the dominance of wind control in large rivers and estuaries toward increasing dominance of water current velocity and depth in smaller channels.

A variety of approaches have been applied to estimate gas transfer velocities in streams and rivers (Devol et al., 1987; Clark et al., 1994; Holtgrieve et al., 2010; Alin et al., 2011; Hall Jr. & Madinger, 2018). Data from these approaches have led to empirical relationships between k and bulk flow properties including channel slope, discharge, mean flow speed, and water depth (Raymond et al., 2012; Natchimuthu et al., 2017; Wallin et al., 2018; Ulseth et al., 2019). Although these parameterizations have mainly been derived for streams, they are applied to larger streams and rivers because direct measurements of k in large rivers are currently lacking, or restricted to estuaries and tidal rivers. Moreover, the contributions of the different mechanisms that generate near-surface turbulence in rivers have not been analyzed quantitatively.

Worldwide many rivers are altered and regulated for human demands (Grill et al., 2019). River regulation is characterized by anthropogenic control of the water level and discharge by dams. Hence, flow regulation is associated with alterations of the magnitude and temporal dynamics of flow velocity (Poff et al., 2007) and can be expected to affect gas exchange.

In this study we aim to identify the key drivers for near-surface turbulence in a regulated river and their temporal variations from hourly to seasonal time scales. Based on intensive field observations in a subarctic river, we quantify the contribution of turbulence generated by bottom shear and from atmospheric forcing (wind shear, buoyancy flux, surface waves) to energy dissipation rates near the water surface. We compare our observations to dissipation estimates obtained from bulk parameters using commonly applied scaling relations, as well as to predictions made by a one-dimensional numerical turbulence model. Based on our findings, we derive a mechanistic concept for quantification of the contributions of flow velocity and wind shear to near-surface turbulence, which can be applied to a range of river sizes.

2 Materials and Methods

2.1 Site description

The present study was conducted in summer 2018 as part of the KITEX experiment, which was an international measurement campaign, designed to improve the understanding of river-atmosphere greenhouse gas exchange. The study combines atmospheric and water-side measurements throughout the ice-free season (June to September) in a regulated river located in continental subarctic climate.

The study was conducted in the River Kitinen, 5 km south of the town Sodankylä in Northern Finland (67.3665°N, 26.6230°E; Figure 1a,b). At our study site, the river is a Strahler order 5 river according to HydroSHEDS database (Lehner et al., 2008). The River Kitinen is the main tributary of the River Kemijoki, which is the longest (ca. 600 km) river in Finland. The construction of two large reservoirs, Lokka and Porttipahta, in the drainage area (ca. 51 000 km^2) of the River Kitinen in 1960, as well as seven hydroelectric power plants, modified the river hydrology drastically. One of the consequences is that the spring flooding is no longer present (Åberg et al., 2019). The power company regulates the river discharge at the power stations in such a way that the production of hydroelectricity increases in the morning and decreases during the night every day. In addition, less electricity is generated on the weekends than on weekdays (Krause, 2011).

The measuring site was located between the two operating power plants: Kelukoski (ca. 10 km) to the north and Kurkiaska (ca. 10 km) to the south (Figure 1b). The river width at the study location was 181 m and the maximum water depth was 6 m. A floating platform 6 m long and 3 m wide with measurement instruments was installed near the middle of the river where the river depth reached 4.5 m. The platform had an anchor system with underwater buoys in each corner. Such a construction made the measurement platform more stable in presence of surface waves.

An eddy covariance (EC) mast was installed at the bank of the river, at a distance of approximately 80 m from the platform. Additionally, meteorological data were collected at meteorological station located at about 247 m east from the floating platform and operated by the Finnish Meteorological Institute (FMI).

2.2 Water-side measurements

The instruments and their deployment configurations of the water-side measurements are summarized in Table 1 and Figure 1. An Acoustic Doppler Velocimeter (ADV Nortek Vector) was installed twice during the measurement campaign. For the first month (10 June to 10 July 2018) it was deployed at the northern (upstream) side of the platform and at the western side for the remaining period (10 July to 24 September 2018). The ADV was installed oriented downwards at a water depth of 0.24 – 0.25 cm in both deployments, providing continuous measurements of flow velocity, from which turbulence can be calculated at a fixed depth of 0.4 m below the water surface. An upward-oriented Acoustic Doppler Current Profiler (ADCP RDI Workhorse 600 kHz) was deployed at the the bottom of the river, approximately 10 m upstream of the platform. Its profiling range extended from $\sim$ 0.7 m above the bottom (including the blanking distance of 0.2 m and the instrument height of 0.4 m) to $\sim$ 0.3 – 0.4 m below the surface with a vertical resolution of 0.1 m. The ADCP operated in pulse-coherent mode (high-resolution water profiling mode) and provided vertical profiles of mean flow velocity and turbulent velocity fluctuations. A thermistor chain was deployed to measure water temperature at 5 different depths (Table 1). Water level fluctuations and surface waves were observed using a wave recorder (RBR duet), which was rigidly deployed at the EC mast at 0.4 m below the water surface. Photosynthetically active radiation (PAR) was measured at the platform at three different water depths. It was used to estimate the attenuation coefficient (k_d [m^{-1}]) in water at noon using the Beer-Lambert law. In addition, we used the daily mean discharge and water level measurements provided by the Kurkiaska power station located downstream from the study site (source of data: Finnish Environment Institute SYKE / Hydrologian ja vesien käytön tietojärjestelmä HYDRO, available at `http://www.syke.fi/avoindata`, last access: 03.01.2019).

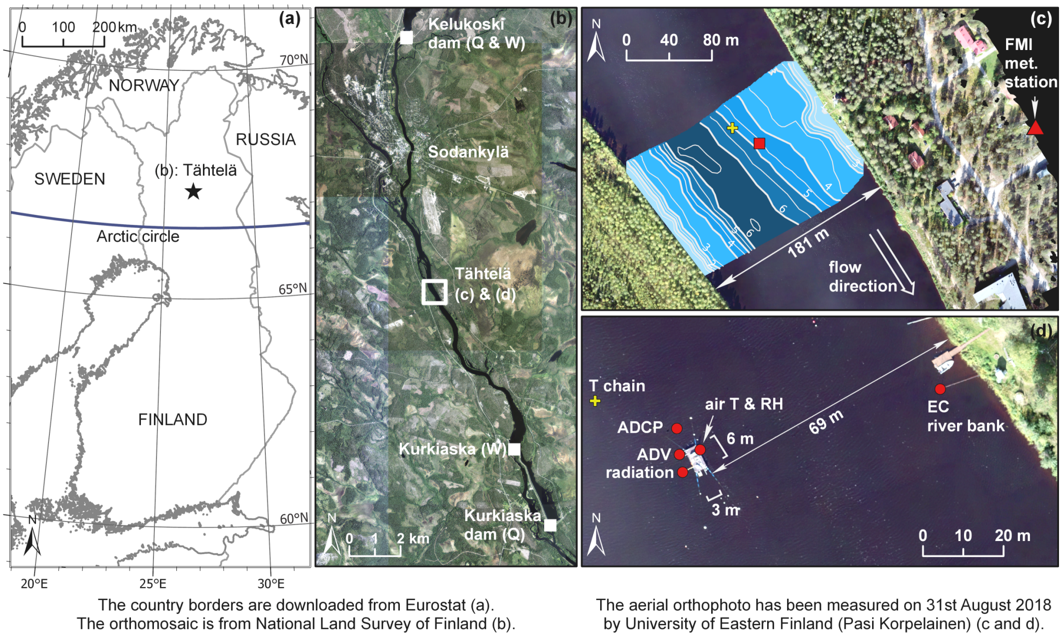

Figure 1. Location of the River Kitinen and the study site (a) – (b). The study site is marked by the black star in (a) and by the white box in (b). (c) shows the river bathymetry at the study site, text labels refer to water depth in meter. The yellow and red symbols mark the location of the thermistor chain (also in (d)) and floating platform, respectively. The red triangle indicates the location of the land meteorological station operated by the Finnish Meteorological Institute (FMI). (d) Areal photograph of the instrument platform and locations of instruments. The red circles show the locations of the acoustic Doppler velocimeter (ADV), acoustic Doppler current profiler (ADCP), air temperature, relative humidity and radiation sensors and eddy covariance (EC) mast.

2.3 Air-side measurements

The meteorological measurements are summarized in Table 2. The eddy covariance system included a USA-1 (METEK) three-axis sonic anemometer/thermometer, which was mounted on a mast in the river at a distance of 10 m from the river bank and at a height of 2 m. The EC system provided mean wind speed $\overline{u}_{wind}$ [m s^{-1}], wind direction w_{dir} [°] and wind friction velocity $u_{*a,EC}$ [m s^{-1}] at 2 m height. The first two were gap-filled using linear regression between the data from the platform and the land station data. We used incoming shortwave and longwave radiation from the land station, which were nearly identical to the values measured at the platform, but without gaps. The outgoing shortwave radiation was calculated as a product of albedo and incoming shortwave radiation, where albedo was estimated from Fresnal's Law (Neumann & Pierson, 1966). Outgoing longwave radiation was calculated as a function of water surface temperature. Air temperature and relative humidity were measured at the platform (Rotronic HC2-S3CO3), and were gap-filled using linear regression between the platform data and the land station data.

Table 1. Water-side measurements conducted in the River Kitinen

Parameter	Instrument	Period of measurements	Sampling frequency [Hz]	Depth of deployment [m]
Flow velocity	ADV Nortek Vector	10 June to 24 September 2018	32	~ 0.4
Velocity profile	ADCP RDI Workhorse 600 kHz	7 June to 10 September 2018	1-1.5	~ 4.2
Water level measurements	RBR duet	10 June to 24 September 2018	Wave burst mode: every 5 min 512 measurements with 16Hz	0.43
Water temperature measurements	RBR solo	6 June to 24 September 2018	0.1	6 June to 17 June 2018: 0.35, 1.35, 2.35, 3.35, 4.35 17 June to 24 June 2018: 0.07, 1.05, 2.05, 3.05, 4.05
Photosynthetically active radiation (PAR)	LI-COR LI-192 directional PAR sensor (0.3 m, 1 m); LI-COR LI-193 omnidirectional PAR sensor (0.65 m)	31 May to 2 October 2018	1/60	0.3, 0.65, 1

Table 2. Meteorological measurements conducted at the study site

Parameter	Instrument/ Manufacturer	Period of measurements	Sampling interval	Instrument height [m]	Location
Wind speed, wind direction, wind friction velocity	USA-1 (METEK)	29 May to 17 October 2018	1/10 s	2	River bank
Wind speed, wind direction	UA2D, Adolf Thies GmbH & Co. KG	01 May to 31 October 2018	1 min	22.7	Land meteorological station (FMI)
Incoming short- and longwave radiation	CM11, Kipp & Zonen B.V.	01 May to 31 October 2018	1 min	17.5	Land meteorological station (FMI)
Air temperature Relative humidity	Rotronic HC2-S3CO3	31 May to 20 September 2018	1 min	2	Measurement platform
Air temperature	Pt100 sensor, Pentronic AB	01 May to 31 October 2018	1 min	2	Land meteorological station (FMI)
Relative humidity	HMP155D, Vaisala Oy	01 May to 17 October 2018	1 min	2	Land meteorological station (FMI)

2.4 Data processing

2.4.1 Estimation of near-surface dissipation rates from ADV Data

ADV data were quality-checked by removing measurements with a correlation magnitude less than 50% (a standard statistical measure of velocity data quality (Nortek, 2015)). Outliers were removed following the procedures described in (Goring & Nikora, 2002; Wahl, 2003). Subsequent analysis was performed for 10 min periods. If more than 20% of the data within each period were removed by the quality check, the period was discarded, otherwise the missing data were linearly interpolated. Velocities measured in instrument coordinates were rotated into the direction of the mean flow for each interval. Mean flow velocity was calculated for each 10 min time interval as the mean longitudinal velocity component $\overline{u}_{flow}$ [m s^{-1}]. In total, 11% of the data were removed during quality screening and averaging.

Dissipation rate of turbulent kinetic energy ε_{ADV} [W kg^{-1}] was estimated using the inertial dissipation technique also known as inertial subrange fitting (ISF), following (Bluteau et al., 2011). Only the vertical velocity component was considered for the calculation of the dissipation rate due to larger noise contamination in the horizontal velocity components:

$$\varepsilon = \left(\frac{E_{ww}(k)}{A_w \alpha_K k^{-5/3}} \right)^{3/2}. \tag{1}$$

Here, E_{ww} [m^3 s^{-2} rad^{-1}] is the one-sided energy spectrum for the vertical velocity component w, $\alpha_K = 1.5$ [–] is the Kolmogorov constant, k is the wave number [rad m^{-1}], and $A_w = \frac{4}{3} \times \frac{18}{55}$ [–] is a constant (Pope, 2000).

Velocity power spectra in the frequency domain $S_{ww}(\omega)$ [m^2 s^{-1} rad^{-1}] were calculated using Welch's method, after linear detrending and applying a Hanning window to each 10 min segment (number of samples used for the fast Fourier transform: 8192). We converted the spectra from frequency to the wave number space ($\omega = \overline{u}_{flow}k$) using Taylor's frozen turbulence hypothesis, which assumes that the turbulent flow does not change its characteristics while passing through the sensor. The validity of this approach was tested as $\left(\overline{w'^2}\right)^{\frac{1}{2}} / \overline{u}_{flow} \leqslant 0.15$, where w' is turbulent velocity fluctuations in vertical direction.

The spectral range that was used for inertial subrange fitting was limited by the instrument noise at an upper frequency limit ω_{up} [rad s^{-1}] and by the size of energy-containing eddies at an lower wave frequency limit ω_{low} [rad s^{-1}]. We defined the upper cutoff frequency as the frequency for which the ratio of power spectral density to the noise level became smaller than one. The noise level was calculated for each spectrum as the logarithmic mean of S_{ww} at frequencies larger than 50 rad s^{-1} where noise was always observed even for high flow velocity, see Figure 2a.

Many spectra had a pronounced peak caused by surface waves ($\sim$ 10 rad s^{-1} or 1 s period, see Figure 2b). For these spectra, an upper frequency limit for ISF was defined as the frequency where the function $f = S_{ww} \cdot \omega$ had a minimum value within the interval $0.5 \leqslant \omega_{up} \leqslant 3$ [rad s^{-1}]. The lower frequency limit ω_{low} was estimated by identifying a breakpoint in spectral slope at the beginning of the inertial subrange in each spectrum (see SI, Text S1).

Following the suggestions in Bluteau et al. (2011), we applied the following quality criteria to the inertial subrange fits: (1) validity of Taylor's frozen turbulence hypothesis (9.3% of the fittings were rejected); (2) coefficient of determination should be larger than 0 (17% of fits were rejected). In addition, the following optional quality criterion was applied: (3) length of the fitted inertial subrange. 13% of data were rejected due to the length being less than 1/2 of a decade, 5.3 % – 1/3 of decade, 1.6% – 1/5 of decade. We applied the three criteria to all the data (the threshold for the last one was 1/3 of a decade) and rejected fits were discarded from further analyses of dissipation rates.

In the presence of surface waves, the low-frequency end of the inertial subrange was often masked completely by the wave peak, and fitting of the inertial subrange at lower frequencies was not possible (see SI Figure S2b). In these cases, the inertial subrange was fitted for frequencies higher than the wave frequencies, where advection by wave orbital velocities had to be taken into account:

$$\varepsilon = \exp\left\langle \ln\left(\frac{(S_{ww}(\omega) - \text{Noise}\quad\text{level})\,\omega^{5/3}}{\alpha_K J_{ww}}\right)^{3/2}\right\rangle, \tag{2}$$

where $J_{ww} = f(\sigma_1, \sigma_2, \sigma_3, \overline{u}, \overline{v})$ is a function describing the effect of the wave advection in terms of the standard deviations of all three velocity components σ, and mean horizontal flow velocities $(\overline{u}, \overline{v})$ (Gerbi et al., 2009). The angled brackets denote averaging over all frequencies ω for which the inertial subrange fit was applied. This method is a slightly modified version of the one proposed by (Feddersen et al., 2007). The range of the frequencies was selected manually for all wave peaks. Unfortunately, we could not find any working criteria for identification of the wave peak in spectra as the wave existed at varying amplitudes during all type of flow conditions. Hence, we manually selected spectra that were affected by surface waves and for which no inertial subrange (or with not sufficient length) was observed at frequencies lower than the wave peak. These selected spectra were fitted according to Eq. (2). A comparison of both fitting procedures for spectra where an inertial subrange could be fitted at both sides of the wave peak, revealed good agreement of the resulting dissipation rates (see Figure 2b). 50% of the total data were analyzed using using Eq. (1) (of which 27% were removed by the misfit criteria). 37% of the data were analyzed using Eq. (2), while the remaining 13% of 10 min intervals were discarded during the initial quality screening.

To exclude time periods for which the observed flow was potentially affected by the platform, we discarded dissipation rate estimates for which the sampling location was at the downwind end of the platform, i.e. for wind direction (1) $80° \leqslant w_{dir} \leqslant 245°$ for the first and (2) $20° \leqslant w_{dir} \leqslant 150°$ for the second deployment. This led to a further 22% reduction of the quality-checked data resulting in 7012 dissipation rate estimates.

2.4.2 Estimation of dissipation rates from ADCP data

We used the following procedure for ADCP data screening and analysis. Measurements with a magnitude of signal correlation less than 70 were removed and velocity time series at each depth were despiked using the same parameters as for the ADV data. For the first 33 days, we applied a bin mapping procedure using linear interpolation (Ott, 2002) due to a significant instrument tilt during this deployment ($\sim 8°$). Frequently occurring losses of connection to the ADCP resulted in missing data and a slight reduction of actual sampling frequency. If the number of missing velocity measurements in 10 min analysis intervals was less than 20%, we applied linear interpolation to fill these gaps using the mean sampling frequency for this period.

Velocities were measured in beam coordinates, which were transformed to orthogonal (instrument) coordinates before being rotated into the mean flow direction (longitudinal, transversal and vertical velocity components) for 10 min averaging intervals. After quality screening and averaging, the total number of valid velocity measurements was $\sim 50\%$ in the middle of the water column and slightly less (44%) near the water surface (0.4 m water depth).

Frequency spectra were calculated from beam velocities over 10 min periods (number of samples used for the fast Fourier transform: 256) and log-averaged over all 4 beams $S(\omega)$ [m^2 s^{-1} rad^{-1}]. The interpolation in cases mentioned above affected the high-frequency part of the spectra, and we excluded all frequencies larger than 2.2 rad s^{-1}. The identification of the lower and upper frequencies of the inertial subrange is described in SI, Text S2.

Since the ADCP cannot resolve the direction of the turbulent velocity fluctuations which were measured in along-beam directions, the isotropy constant A (Eq. (1)) is undetermined. In this study the isotropy constant was set to 1 following Lorke and Wüest (2005).

We applied the same quality criteria to spectral fits as for the ADV data. Comparisons of velocity spectra from both instruments and corresponding inertial subrange fits are exemplarily shown in Figure 2. The dissipation rate estimates from both instruments agreed on average but, depending on optional quality screening criteria, individual estimates differed by several orders of magnitude. A more detailed comparison of dissipation rate estimated from both instruments is provided in SI, Text S3, Figure S3.

Since the sampling frequency of the ADCP was too small to resolve wave orbital velocities, we could not estimate the dissipation rate during the wave-affected periods. On the other hand, the ADV resolved the vertical velocity component directly and had higher quality data. Therefore, we primarily used the ADV measurements for the calculation of the near-surface dissipation rate in the following sections. The ADCP based estimates are used in sections (e.g. Section 2.6, 3.3) where we specifically analyze bottom-generated turbulence and vertical profiles of the dissipation rate.

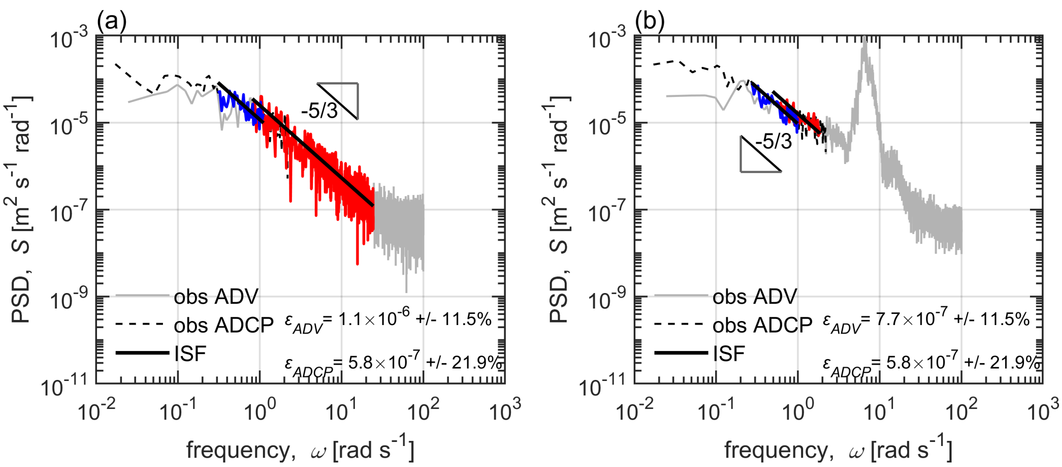

Figure 2. Typical frequency spectra (power spectral density, PSD) of vertical velocity fluctuations measured by ADV (grey line) and of along-beam velocity fluctuations measured by ADCP (dashed black line): (a) for a period without surface waves and (b) for a period with surface waves (wave peak at around 10 rad s^{-1}). Blue and red parts of the spectra represent the selected range for estimating dissipation rates by inertial subrange fitting (ISF, -5/3 slope) for ADCP and ADV, respectively. Black lines show the corresponding fits. The dissipation rates obtained from ISF ε_{ADV}, ε_{ADCP} with confidence bands are provided as labels.

2.4.3 Eddy covariance

A double rotation of the coordinate system was performed with the wind velocity measurements of the anemometer (McMillen, 1988). The atmospheric friction velocity was calculated from the original 10 Hz data as 5 min block-averages:

$$u_{*,SBL,EC} = \left(\overline{u'w'}^2 + \overline{v'w'}^2\right)^{\frac{1}{4}}. \tag{3}$$

Screening for weak turbulence with a specific friction velocity limit was not performed, but the cases with upward momentum flux ($\overline{u'v'} > 0$) were discarded. The 5 min $u_{*,SBL,EC}$, wind speed and wind direction data were further averaged to 10-min mean values to enable direct comparison with other data. Acceptable wind directions were $151° \leqslant w_{dir} \leqslant 190°$ and $290° \leqslant w_{dir} \leqslant 323°$ to ensure sufficient fetch with an open water surface.

2.5 Turbulence from atmospheric forcing

To estimate dissipation rates in the water from bulk measurements of atmospheric forcing, we used the atmospheric similarity scaling described in Tedford et al. (2014). During periods of heating of the water surface (the surface buoyancy flux, $J_{BO} > 0$ [W kg^{-1}]), dissipation rates were estimated as:

$$\varepsilon_{SBL} = \varepsilon_{SBL,wind} = 0.6\frac{(u_{*SBL})^3}{\kappa z}, \tag{4}$$

where $\kappa = 0.41$ [–] is the von Kármán constant, z [m] is the distance from the water surface, u_{*SBL} [m s^{-1}] is the water friction velocity computed from wind shear stress τ_a [N m^{-2}] as $u_{*SBL} = (\tau_a/\rho_w)^{1/2}$, ρ_w [kg m^{-3}] is the water density. Wind shear stress is calculated from the wind speed as $\tau_a = \rho_a C_{Da}\overline{u}_{wind}^2$, where C_{Da} [–] is the drag coefficient, ρ_a [kg m^{-3}] is the air density. We assumed a neutral drag coefficient at 10 m height of $C_{DaN,10m} = 1.3{\cdot}10^{-3}$, which we corrected for the 2 m measurement height of $C_{DaN,2m} = 1.8{\cdot}10^{-3}$ using boundary-layer scaling. This value was corrected for the stability of the atmosphere following (Hicks, 1972).

The buoyancy flux was calculated as $J_{BO} = g\alpha Q_{heat}/(C_{pw}\rho_w)$, where Q_{heat} is the effective heat flux, α the thermal expansion coefficient of water, C_{pw} [J kg^{-1} °C^{-1}] is the specific heat capacity of water, and g [m s^{-2}] is the gravitational acceleration. The surface heat flux was computed as the sum of latent heat flux, sensible heat flux and net longwave radiation, and the effective heat flux for the actively mixing layer as the sum of the surface heat flux plus the shortwave radiation retained within the actively mixing layer. The mixed layer depth was estimated as the depth where the water temperature difference from the surface is 0.02°C. All calculations above were based on formulations from (MacIntyre et al., 2002, 2014).

During water cooling ($J_{BO} \leqslant 0$), when convective mixing also contributed to the dissipation rate, ε_{SBL} was estimated as:

$$\varepsilon_{SBL} = \varepsilon_{SBL,wind} + \varepsilon_{SBL,buoy} = 0.56\frac{(u_{*,SBL})^3}{\kappa z} + 0.77|J_{BO}|. \tag{5}$$

Additionally, we used surface boundary layer scaling to estimate wind-generated energy dissipation rates in the water from atmospheric momentum fluxes measured by EC:

$$\varepsilon_{SBL,EC} = \frac{(u_{*,SBL,EC})^3}{\kappa z}, \tag{6}$$

where the water-side friction velocity $u_{*,SBL,EC}$ was estimated from the friction velocity in air $u_{*a,EC}$ obtained from the EC system as $u_{*,SBL,EC} = u_{*a,EC}\,(\rho_a/\rho_w)^{1/2}$.

2.6 Bottom-generated turbulence

We estimated the bed friction velocity in the bottom boundary layer u_{*BBL} [m s^{-1}] by fitting the observed vertical profiles of the mean flow velocity measured by the ADCP to the law of the wall as

$$\overline{u}_{flow} = \frac{u_{*BBL}}{\kappa} \ln \frac{h}{z_0}, \tag{7}$$

where z_0 [m] is the hydrodynamic roughness length and h [m] is the distance from the bottom. Visual inspection of velocity profiles provided an approximate height below which the logarithmic profile was valid of ~ 2.4 m above the river bed. As an initial guess, we used a fixed value of $z_0 = 0.0017$, which corresponds to a Manning's roughness coefficient $n_M = 0.026$ s m$^{-1/3}$ for a coarse sand channel (Chow, 1959; Arcement & Schneider, 1989) and the bed drag coefficient $C_{Dw} = 0.0041$ at 1 m above the bottom. To estimate the near-surface turbulence caused by the bottom friction, we computed the dissipation rate of turbulent kinetic energy using the law of the wall:

$$\varepsilon_{BBL,wall} = \frac{(u_{*BBL})^3}{\kappa h}. \tag{8}$$

This approach is based on the assumption that the shear stress is constant over the entire water column and equal to bed shear stress. An alternative approach, which is based on the assumption of linearly decreasing shear stress from the bed to zero at the water surface (Nezu, 1977), results in a stronger exponential scaling of dissipation rates with distance from the bed:

$$\varepsilon_{BBL,Nezu} = \frac{(u_{*BBL})^3}{H} \frac{E}{\sqrt{h/H}} \exp(-\frac{3h}{H}), \tag{9}$$

where H [m] is the total water depth ($H = 4.2$ m is the water depth of ADCP deployment), E [–] is an empirical constant for which we assigned a value of $E = 4.76$, as suggested for a smooth river bed by Nezu (1977). Density stratification is not considered in either scaling laws. Vertical profiles of dissipation rates predicted by both approaches were compared with measurements using a range of values of z_0 in order to get the best agreement (Section 3.3). In the following section, the notation $\varepsilon_{BBL,ADCP}$ is used for both approaches in order to underline that that these estimated are based on the ADCP measurements.

2.7 Relative importance of bottom and surface generated turbulence

To identify the dominant mechanisms generating near-surface turbulence, we followed a two-step procedure. At first, we compared the direct estimates of bed-generated turbulence from the ADCP observations ($\varepsilon_{BBL,ADCP}$ from Eq. (8 – 9)) with dissipation rates from atmospheric forcing ε_{SBL} predicted by bulk-scaling (Eq. (4 – 5)) and distinguish between the following four cases:

1. $\varepsilon_{BBL,ADCP} \geqslant \varepsilon_{SBL}$: bottom-generated turbulence is dominant;
2. $\varepsilon_{BBL,ADCP} < \varepsilon_{SBL}$ but $\varepsilon_{BBL,ADCP} > \varepsilon_{SBL,wind}$ and $\varepsilon_{BBL,ADCP} > \varepsilon_{SBL,buoy}$: atmospheric forcing (wind and buoyancy flux combined) is dominant;
3. $\varepsilon_{SBL,wind} > \varepsilon_{BBL,ADCP}$ and $\varepsilon_{SBL,wind} > \varepsilon_{SBL,buoy}$: the wind-generated turbulence alone is dominant;

4. $\varepsilon_{SBL,buoy} > \varepsilon_{BBL,ADCP}$ and $\varepsilon_{SBL,buoy} > \varepsilon_{SBL,wind}$: convectively-generated turbulence alone is dominant.

The computation of $\varepsilon_{BBL,ADCP}$ is based on the ADCP data which were only collected during a relatively short period of time. In a second step, we replace the observed dissipation rate by bulk scaling using mean flow velocity observed by the ADV as it spans a longer period of time:

$$\varepsilon_{BBL,ADV} = \frac{C_{Dw}^{3/2}\overline{u}_{flow}^3}{\kappa(H-z)}. \tag{10}$$

Here, the notation 'ADV' is used because we apply the ADV mean flow velocity. We apply the drag coefficient C_{Dw} obtained from the fitting procedure described in the Section 3.3 and C_{Da} mentioned in Section 2.5.

Finally, we make an attempt to derive a more general solution to distinguish the cases mentioned above. By considering bottom and wind generated turbulence only, the ratio of the the corresponding dissipation rates (Eq. (4), (10)) becomes:

$$\frac{\varepsilon_{BBL}}{\varepsilon_{SBL}} = \frac{u_{*BBL}^3}{\kappa(H-z)}\frac{\kappa z}{u_{*a}^3} = \frac{z}{H-z}\cdot\left(\frac{\rho_w}{\rho_a}\right)^{\frac{3}{2}}\cdot\left(\frac{C_{Dw}}{C_{Da}}\right)^{\frac{3}{2}}\cdot\left(\frac{\overline{u}_{flow}}{\overline{u}_{wind}}\right)^3 \tag{11}$$

Values of the ratio greater than unity indicate that bottom-generated turbulence is dominant. Otherwise, the atmospheric-generated turbulence is dominant. Note, that we do not consider the cases with the dominant buoyancy flux here assuming its contribution is not significant in time. The equation can be used to derive a "critical" wind speed, for which bottom and wind generated dissipation rates are equal, i.e. for wind speeds greater than the critical wind speed, wind is the dominant forcing of near-surface turbulence:

$$u_{wind,crit} = \overline{u}_{flow,1m}\left(\frac{\rho_w}{\rho_a}\right)^{1/2}\left(\frac{C_{Dw,1m}}{C_{Da}}\right)^{1/2}\left(\frac{z}{H-z}\right)^{1/3}. \tag{12}$$

Note, that these estimates are not valid during stable density stratification. We further discuss the implications of these equations in Section 3.5.

2.8 Description of the one-dimensional $k-\varepsilon$ model

Both bottom shear stress and atmospheric forcing are taken into account while simulating dissipation rates below the water surface using a physically sophisticated, spatially resolving turbulence model of river flow. The one-dimensional (in vertical direction) modelling of turbulent river flow should be sufficient to reproduce the vertical structure of thermo- and hydrodynamic properties, if the marginal effects at river banks are negligible; this is the case when depth-to-width ratio is small (about 0.02 for the River Kitinen at the location of experiment). The $k-\varepsilon$ model used in this study is a 1D version of Reynolds-Averaged Navier-Stokes (RANS) equation system. This system is an exact result of spatial averaging of 3D RANS-equations over a horizontal cross-section of a river stream, which shape is assumed to be a parallelepiped (Figure 3), neglecting heat and momentum fluxes at the channel banks and omitting longitudinal advection (see the equations in SI, Text S4). The boundary conditions are as follows:

- momentum flux from the atmosphere at the top ($z = 0$), (τ_x, τ_y), is computed via Monin-Obukhov similarity using on-raft measurements of meteorological variables;

- momentum flux at bottom ($z = H$) is given by logarithmic law with bottom roughness length $z_0 = 2 \cdot 10^{-4}$ m, a value defined in Section 3.3;
- measured water temperature time series at $z = 0$, whereas measured downward radiation fluxes, sensible and latent heat fluxes to the atmosphere computed using Monin-Obukhov similarity are used for calculation of the buoyancy flux at the surface B_s (used below);
- zero heat flux at $z = H$,
- for turbulent kinetic energy K (TKE), the boundary condition is $K = C_{e0}^{-1/2} u_{*s}^2$ at $z = 0, H$, where $C_{e0} = 0.09$ is Kolmogorov constant, u_{*s} is friction velocity at respective boundary, and for dissipation rate, the local equilibrium with turbulent kinetic energy production is assumed:

$$\varepsilon = \frac{u_{*s}^3}{\kappa z_*} + B_s \text{ at } z = 0, H. \tag{13}$$

where $H = 4$ m is the average river depth, z_* is a distance from the first computational node to the boundary. Radiation flux S is given by Beer-Lambert law applied in 4 bands (ultraviolet, photosynthetically-active radiation (PAR), near-infrared, infrared), and attenuation coefficient for PAR set to mean measured value k_d =3 m^{-1}. The full system is solved using LAKE2.0 model code (Stepanenko et al., 2016) as it uses horizontal averaging of thermo- and hydrodynamic equations as well. The only modification to the lake model algorithm is addition of a method to compute a free-surface gradient $\overline{g\partial h_s/\partial x}$, where h_s is free water surface height, x is longitudinal coordinate. We assume dynamic balance between the horizontal pressure gradient force, bottom friction and surface longitudinal momentum flux:

$$-g\overline{\frac{\partial h_s}{\partial x}} = \frac{gU^2 n_M^2}{R_H^{4/3}} - \frac{\tau_x}{H\rho_{w0}}, \tag{14}$$

with R_H denoting hydraulic radius, U standing for u velocity component averaged over a transversal (vertical) cross-section, ρ_{w0} is reference water density, n_M is Manning's coefficient. Here, U is readily computed from the river discharge measured at a dam downstream, and a value $n_M = 5.2 \times 10^{-2}$ s m$^{-1/3}$ is adjusted in order the discharge from solution of the equations (SI, Text S4) to match the discharge at a dam. There are at least two errors caused by using the method described above. First, dynamic balance implied by Eq. (14) may be significantly violated during unsteady flow regimes following everyday opening and closing at the dam. The second source of errors is an assumption that the mean velocity at the measurement location is the same as at the dam, while the gravity wave following dam operations travels at a finite speed and thus there is a time lag between abrupt velocity changes at the dam and at the study site. However, estimating phase speed $\sqrt{gH} \approx 6.3$ m/s and given a distance from measurement point to the dam $\sim$10 km downstream, we get 25 min travel time of a wave induced by dam operations to reach the raft, which is small compared to time interval between these operations.

The model was solved for 20 layers in the vertical and 10 s time step.

2.9 Statistical parameters and tests

In this study, we use statistical parameters and tests listed in Table 3.

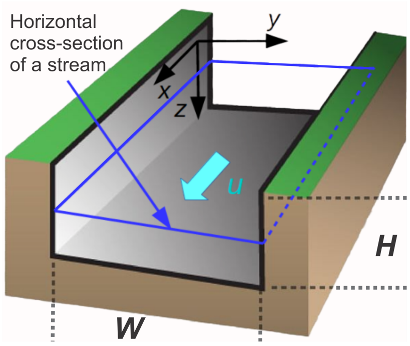

Figure 3. Schematic of a river channel geometry assumed in 1D $k - \varepsilon$ turbulence model

Table 3. Statistical parameters and tests used in current study.

	Parameter	Description
	n	Number of data points (10 min sampling intervals)
	μ	Mean value of the logarithmic ratio of predicted and observed dissipation rates
	ρ	Correlation coefficient
	p	Significance level for the correlation coefficient: significant if $p < 0.05$
Error estimation for dissipation rate (Section 3.3)	Error R	$R = 10^{\left\langle (\log_{10} \varepsilon_{pred} - \log_{10} \varepsilon_{obs})^2 \right\rangle}$ where ε_{pred}, ε_{obs} is the predicted and observed dissipation rate, respectively
Statistical test	–	Two-sample Kolmogorov-Smirnov test

3 Results

3.1 Overview of the measurements

The variations of wind speed, flow velocity and surface buoyancy flux as the main drivers for near-surface turbulence are shown in Figure 4. Wind speed varied between 0 and 8.4 m s^{-1} and often showed a diel pattern with higher values during daytime and lower values during night. Mean flow velocity measured at 0.4 m below the water surface by the ADV varied between 0.001 and 0.34 m s^{-1}. Discharge regulation by the downstream dam operation for hydropower production caused pronounced diel variations of the flow velocity throughout the entire measurement period. River discharge at the downstream Kurkiaska power station (Figure 4b) varied between 1 and 166 m^3 s^{-1}, with no pronounced seasonal pattern. The mean discharge during the time period from 1 June to 30 September was 84 m^3 s^{-1}. Daily mean flow velocity observed by the ADV and the discharge were strongly correlated ($\rho = 0.9$, $p < 0.05$). The surface buoyancy flux generally showed a pronounced diel pattern with seasonally varying amplitude. Maximum ($3.2 \cdot 10^{-7}$ W kg^{-1}) and minimum ($-1.7 \cdot 10^{-7}$) values were observed at the beginning of August. Nighttime buoyancy fluxes were negative throughout the observational period as expected and indicative of convective mixing conditions. The dissipation rate at 0.4 m depth varied between $2.6 \cdot 10^{-9}$ and $1.2 \cdot 10^{-5}$ W kg^{-1} (Figure 4d). Low dissipation rates, less than 10^{-8} W kg^{-1}, were observed when flow velocities were low, i.e. at low discharge. In general, dissipation rates followed the rapid diurnal changes in flow velocity.

Air temperature varied between -0.8°C on September 15 and 30.3°C on July 13 and also showed a diel pattern (Figure S4a). Surface water temperature (at 0.35 m and 0.07 m depth for the first and the second deployments, respectively) increased during summer, reaching its maximum value of 23°C on August 2, and slowly decreased towards autumn to the minimum value of 8.7°C on September 22. Weak thermal stratification developed primarily during the first half of the summer June – July (Figure S5). The maximum value of temperature difference between the surface and bottom (at 4.35 m and 4.05 m depth for two deployments, respectively) reached 2.3°C on June 18 (Figure S5a).

Significant wave height H_{sig} varied with wind speed ($\rho = 0.7$, $p < 0.05$) and was mostly below 5 cm reaching a maximum value of 11 cm (Figure S4c). Unexpectedly, we found weaker correlation between H_{sig} and $\overline{u}_{wind}$ when the wind blew along the main flow direction ($\rho = 0.5$, $p < 0.05$, Figure S6a) in comparison with a relatively strong correlation and linear relationship ($\rho = 0.8$, $p < 0.05$) when the wind direction was opposite the main flow direction (Figure S6b).

The diel dynamics were largerly goverened by flow velocity (Figure 5). The flow velocity was characterized by large-amplitude and rapid sub-daily flow variations with high values usually occurring during daytime and low values during night (Figure 5b,c). The change from high to low flow velocity occurred rapidly. Mean flow velocity often decreased by 50% within 30 to 60 minutes. Depending wind and flow velocity, the direction of the mean flow near the water surface was aligned either with the wind direction, or with the direction of river flow (Figure 5a). During the day, when flow velocities and wind were elevated, incoming heat was sometimes mixed throughout the water column and temperatures increased; on other days temperature declined. If both flow and wind were lower in the day, stratification sometimes developed. After flow speed and wind speed decreased at night, weak thermal stratification occurred and persisted until midnight (see 1-2 July in Figure 5d). Stratification usually persisted for several hours, before it was disrupted by a rapid increase in flow or by convective mixing.

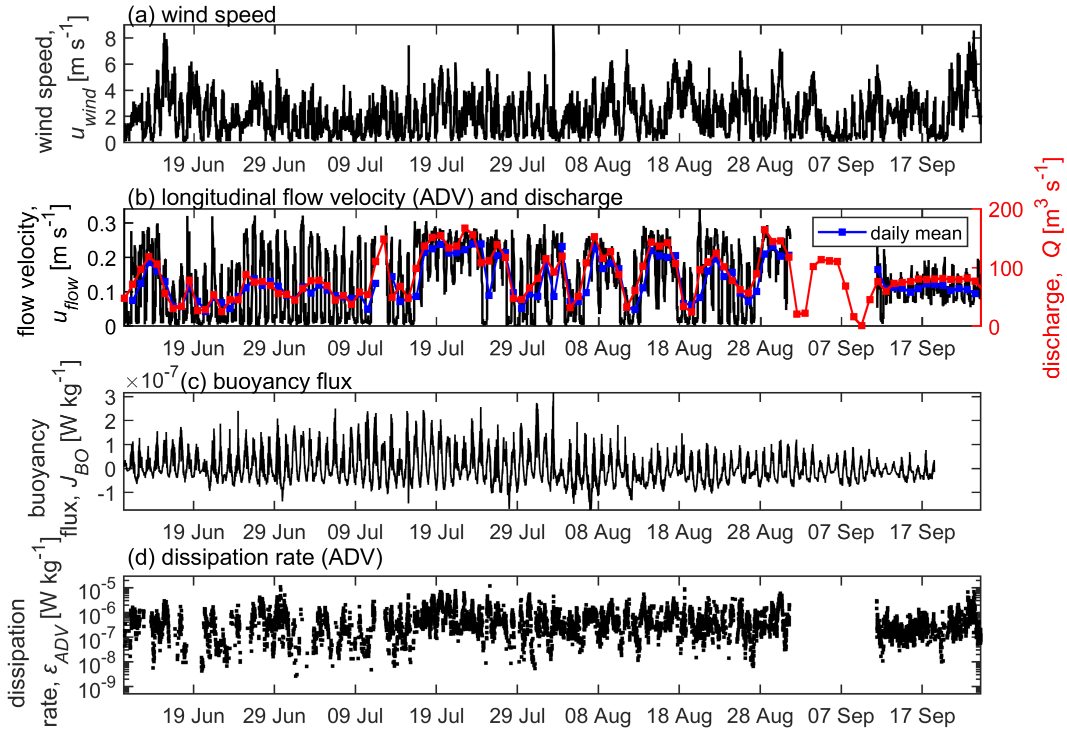

Figure 4. Time series of main drivers of near-surface turbulence during the study period: (a) wind speed (temporal resolution is 10 min); (b) longitudinal flow velocity at 0.4 m water depth (ADV) with a temporal resolution of 10 min (black line), daily mean flow velocity (blue line) and daily mean discharge at Kurkiaska power station (red line with square symbols); (c) buoyancy flux; (d) dissipation rate of turbulent kinetic energy at 0.4 m depth (ADV, temporal resolution of 10 min).

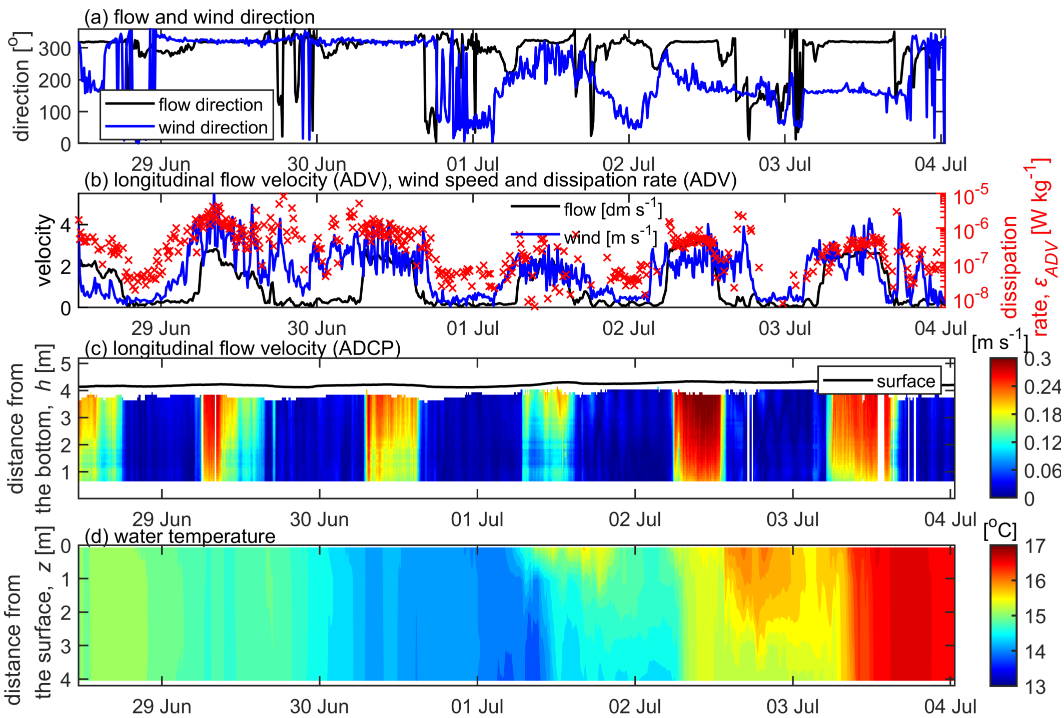

Figure 5. Time series of (a) flow direction (ADV, black line) and wind direction (blue line); (b) flow velocity (ADV, [dm s^{-1}], black line), wind speed ([m s^{-1}], blue line) and dissipation rate of turbulent kinetic energy (ADV, red crosses); (c) flow velocity profiles (ADCP), black line represents water surface; (d) vertical profiles of water temperature. The selected period is from 28 June to 04 July 2018, emphasizing diel dynamics with a temporal resolution of 10 min.

3.2 Turbulence generated by atmospheric forcing

Bin-averaged dissipation rates of turbulent kinetic energy predicted from bulk atmospheric forcing ε_{SBL}, (Eq. (5)) agreed reasonably with observed dissipation rates ε_{ADV} at 0.4 m depth. Deviations between individual 10 min estimates, however, were large and covered several orders of magnitude (Figure 6a). Particularly for lower dissipation rates ($< 10^{-7}$ W kg^{-1}), predicted values were systematically smaller than the observations. The bin-averaging procedure is described in SI, Text S5, Figure S7. Considering only data for which the wind directions was along the river ($151° \leqslant w_{dir} \leqslant 190°$ and $290° \leqslant w_{dir} \leqslant 323°$) did not improve the agreement significantly (a two-sample Kolmogorov-Smirnov test showed no significant difference between them) and did not reduce the systematic deviation between the measured and predicted dissipation rates. The logarithmic ratio of two dissipation rates had a mean value μ = -0.4 in both cases (Figure 6b), indicating that the mean near-surface dissipation rate was 2.5 times higher than predictions from bulk atmospheric forcing.

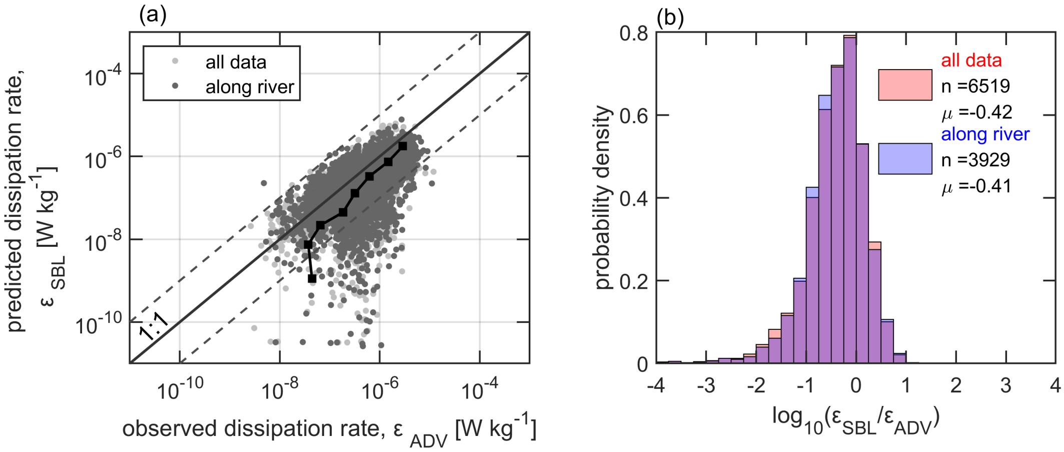

Figure 6. (a) Predicted dissipation rate of turbulent kinetic energy from bulk meteorological forcing ε_{SBL} versus observed dissipation rate ε_{ADV} at 0.4 m water depth. Light grey symbols show all data, dark grey symbols mark data for which the wind direction was along the river ($151° \leqslant w_{dir} \leqslant 190°$ and $290° \leqslant w_{dir} \leqslant 323°$). The black line with square symbols shows bin averaged data. The solid grey line shows the 1:1 relation and two dashed lines indicate differences of one order of magnitude. (b) Probability density distributions (bar graphs) of the logarithmic ratio of ε_{SBL} and ε_{ADV} for two cases: considering all data (red), considering the data with wind directions along river (blue). The number of data points n and the mean value μ are provided in the legend.

In contrast to the predictions from bulk atmospheric forcing, the dissipation rate estimated from measured momentum fluxes by the EC system $\varepsilon_{SBL,EC}$, (Eq. (6)) were on average higher than measured dissipation rates (Figure 7). The contrasting low and high bias of the two dissipation rates estimated from atmospheric forcing were related to the difference between measured wind friction velocity and that estimated from mean wind speed in the bulk scaling (Figure 7b), with the latter being consistently smaller than measured values. The agreement between the measured and predicted friction velocities did not improve if only wind directions along the river were considered.

Following (Wang et al., 2013, 2015) (see Appendix A for details), we additionally tested a scaling relation for near-surface dissipation rates under breaking surface waves proposed for large lakes (see Appendix A, SI, Figure S8a) and estimated the dissipation

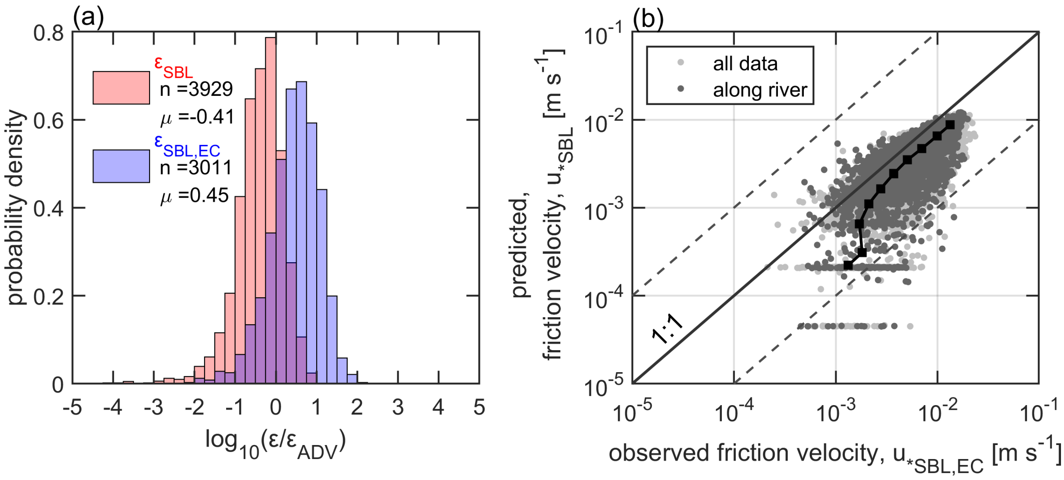

Figure 7. (a) Probability density distributions (bar charts) of the ratio of dissipation rates estimated from atmospheric forcing and observed dissipation rates at 0.4 m depth. The red bars show the distribution for bulk scaling (ε_{SBL}, Eq. (5)) and the blue chart shows the ratio for dissipation rates estimated from measured momentum fluxes by the eddy covariance system ($\varepsilon_{SBL,EC}$ (Eq. (6)). Only data for which the wind direction was along the main river channel river were considered for both distributions ($151° \leqslant w_{dir} \leqslant 190°$ and $290° \leqslant w_{dir} \leqslant 323°$). The number of data points n, mean values of the logarithm of the ratio μ are shown in the legend. (b) Measured wind friction velocity by EC $u_{*SBL,EC}$ versus predicted friction velocity calculated from bulk atmospheric forcing (wind speed) u_{*SBL}. Light grey symbols show all the data, dark grey symbols show data for which the wind directions was along the river. The solid black line indicates a bin-average of the log-transformed data, the grey solid line shows a 1:1 ratio and the two grey dashed lines represent a one order of magnitude difference.

rate by taking measured significant wave height into account. In comparison to dissipation rates predicted from bulk atmospheric forcing (ε_{SBL}), the wave scaling (ε_{wave}) did not improve the prediction quality (mean value of the ratio of ε_{wave} and ε_{ADV} μ = -1.18, see SI, Figure S8b). On average, observed dissipation rates were a factor of 15 higher than the prediction ε_{wave}. The wave contribution to the dissipation rate was small due to much larger relative depth (depth of the dissipation rate measurements over the significant wave height) than in the former observations made in large lakes.

3.3 Bottom-generated turbulence

We estimated the bottom-generated turbulence using Eq. (8) and (9) considering several values of z_0 with the flow velocity $\overline{u}_{flow}$ taken at $h = 1$ m. As the first step, we compared the observed dissipation rate at 1 m above the bed (ε_{ADCP}) with dissipation rates predicted from mean flow velocity and an initial guess of the bed roughness ($\varepsilon_{BBL,wall}$). For small values of the predicted dissipation rates ($< 1 \cdot 10^{-7}$ W kg^{-1}), the observations appeared to be higher than the predictions and uncorrelated, while observations and predictions were correlated for higher dissipation rates (see SI, Figure S9a). By assuming that the dissipation rates in the lower range were additionally affected by atmospheric forcing, we only considered dissipation rates exceeding this threshold in all subsequent analyses. The remaining data (number of data points $n = 950$) were used for fitting the roughness length z_0 by minimizing the error between the predicted and measured dissipation rates (see SI, Table S1). The resulting z_0 was equal to 0.0002 m, corresponding to a Manning's coefficient of $n_M = 0.02$, and a drag coefficient of C_{Dw} =

0.0023 (at 1 m above the bed, Figure 8a). The fitted value of Manning's coefficient was within the range reported by Arcement and Schneider (1989) for the rivers with sand bed and the straight uniform channel where grain roughness is predominant. On average the dissipation rates $\varepsilon_{BBL,wall}$ showed good agreement with observed values ε_{ADCP}. We additionally tested the Nezu approach (see SI, Figure S9b) by using the fitted n_M and by applying a range of values for the empirical constant E, Eq. (9), that has been reported in the literature (see SI, Table S2). The smallest error between observed and predicted dissipation rates at 1 m height above the sediment was obtained value of $E =$ 9.8, which has been originally reported by Nezu (1977).

The log-averaged, mean values of all observed dissipation rates ε_{ADCP} decreased by a factor of three from a maximum value of $1.1{\cdot}10^{-6}$ W kg^{-1} at a distance of 0.7 m above the bottom to ($3.9{\cdot}10^{-7}$ W kg^{-1}) near the water surface (Figure 8b). The mean vertical profile of dissipation rates followed the law of the wall scaling $\varepsilon_{BBL,wall}$ throughout the most of the water column, while the scaling according to Nezu $\varepsilon_{BBL,Nezu}$ showed better agreement with the measurements only near the bottom ($\sim$ 1.2 m). From here on, we use the notation $\varepsilon_{BBL,ADCP}$ referring to the dissipation rate obtained using the law of the wall scaling $\varepsilon_{BBL,wall}$.

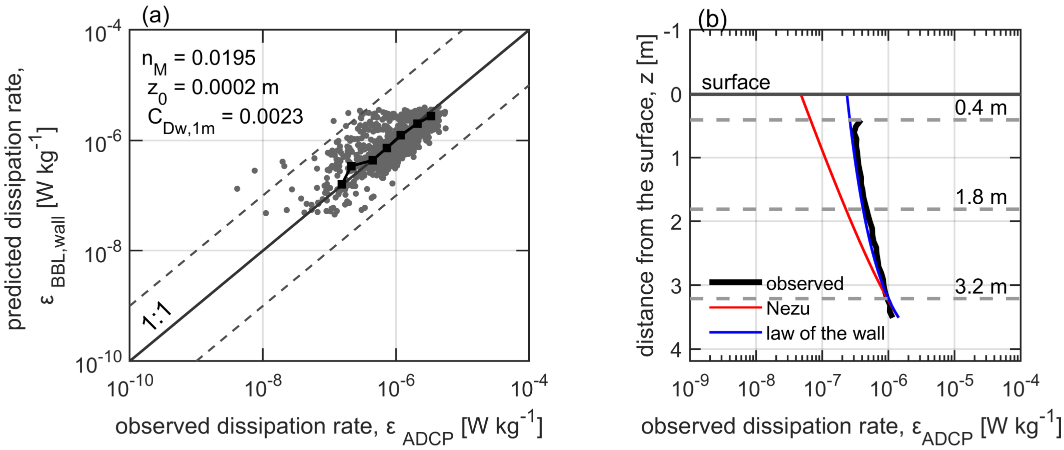

Figure 8. (a) Dissipation rates predicted from mean flow velocity ($\varepsilon_{BBL,wall}$) versus observed dissipation rates ε_{ADCP} at a height of $\sim$ 1 m above the bottom (grey symbols, only data with $\varepsilon_{BBL,wall} > 1 \cdot 10^{-7}$ W kg^{-1} are shown, see SI, Figure S9). The black line with square symbols shows a logarithmic bin average of the data. The solid grey line shows a 1:1 relation and two dashed lines indicate differences of one order of magnitude. (b) Vertical profiles of dissipation rates of turbulent kinetic energy: the black line shows mean (log-averaged) observations. The red line shows the mean dissipation rates estimated using the Nezu approach, and the blue line is the mean dissipation profile according to the law of the wall. The black horizontal line marks the water surface, dashed grey lines correspond to 0.4 m (the depth of the ADV measurements), 1.8 m is the depth below which the u_{*BBL} was calculated, 3.2 m is the depth for which the comparison (a) was done.

3.4 Relative importance of atmospheric forcing and bottom-generated turbulence

To evaluate the contributions of different generation mechanisms to turbulence near the water surface, we compared measurements of bottom-generated turbulence ($\varepsilon_{BBL,ADCP}$ from the ADCP profile measurements extrapolated to 0.4 m water depth) with dissipation rate estimates for wind shear ($\varepsilon_{SBL,wind}$ calculated from mean wind speed) and surface buoyancy flux ($\varepsilon_{SBL,buoy}$ from the surface heat flux). The maximum dissipation rate predicted by either of the three relationships for a water depth of 0.4 m (ADV sampling depth) was used to identify the dominant forcing mechanism and was used as the best predictor.

To extend the identification of dominant forcing mechanisms to the time periods without valid ADCP measurements, we used the dissipation rate computed from the bulk formula using the mean flow velocity measured by the ADV and the estimated bottom drag coefficient (corresponding to z_0 from Section 3.3, $\varepsilon_{BBL,ADV}$, Eq. (10)). We calculated the percentage corresponding to the dominance of $\varepsilon_{SBL,wind}$, $\varepsilon_{SBL,buoy}$ and both $\varepsilon_{BBL,ADCP}$ and $\varepsilon_{BBL,ADV}$ (see Table 4). We found no significant difference between the percentages if we used valid subsections ADCP or ADV dissipation estimates for bottom-generated turbulence.

For the time periods with ADV observations, bottom-generated turbulence dominated for 43% of the time, wind 42%, and convective cooling 14% of the time. The remaining data with $\varepsilon_{BBL,ADV}$ larger than $\varepsilon_{SBL,wind}$ and $\varepsilon_{SBL,buoy}$, but smaller than their sum, were only 1.4% of total cases and are not included in further analyses. The predicted dissipation rates agree well with our observations ($\rho = 0.5$, $p < 0.05$, Figure 9a). The mean value of the ratio of predicted and observed dissipation rates was 0.9.

When considering only wind and bottom-generated turbulence quantified from wind speed and and mean flow velocity, respectively (Eq. (11)), the statistics of the dominant forcing changes only slightly. Wind and bottom generated turbulence dominated in 62% and 38% of total time, respectively (Table 4). Considering the previous computation, the dominance of $\varepsilon_{SBL,buoy}$ would be responsible for approximately 15% of the atmospheric cases.

Wind shear affected near-surface dissipation rates for wind speeds greater than 1 m s^{-1} and was the dominant mechanism for wind speeds exceeding 3 m s^{-1} (Figure 9b). When the flow velocity exceeded 9 – 10 cm s^{-1}, the bottom generated turbulence dominated the near surface energy dissipation (Figure 9c). The contribution of the buoyancy flux was important at night, when the convective cooling coincided with low flow velocity and low wind speed. It was the most frequent cause of turbulence at wind speed less than 2 m s^{-1} and flow velocities less than 9 – 10 cm s^{-1}.

Thermal stratification may affect the dependence of near-surface dissipation rates on bulk forcing variables. Following (Bormans & Webster, 1997), we used a temperature difference between the surface and bottom water exceeding 0.05°C to identify periods of thermal stratification. We compared the probability density distributions of the ratio of predicted and observed dissipation rates for cases when wind, flow, and buoyancy flux were the dominant forcing mechanisms (Figure S10). Significant differences between situations with and without stratification were found for cases when wind and flow were the dominant drivers. During the stratified conditions, the predicted dissipation rates for wind and bottom-generated turbulence were smaller by 18% and 21%, respectively, than during the unstratified conditions.

To test the effect of wind direction relative to the flow direction on near-surface dissipation rates, we separated the data when the wind directions was along ($290° \leqslant w_{dir} \leqslant 323°$) and against ($151° \leqslant w_{dir} \leqslant 190°$) the longitudinal river flow. Significant difference were found between these two cases for the situations when the wind or flow was the dominant forcing mechanism (Figure S11). For wind-generated turbulence, the predictions were underestimating near-surface dissipation rates by 16% for the periods when wind direction was along river flow in comparison to the periods when wind direction was against the river flow. For bottom-generated turbulence, the predicted dissipation rates were higher than observed by 17% for wind direction against the river, while they were lower by 19% when the wind was directed along the river flow. Nevertheless, these effects were small compared to the large uncertainty in dissipation rate measurements. The cumulative uncertainties in the measurement related to dissipation rates has been estimated to be within a factor of two (Moum et al., 1995). The presence if surface waves, an their effects on inertial subrange fitting, probably added to this uncertainty.

Table 4. Relative contribution of different predicted dissipation rates and different measurements. The first column represents the maximum magnitude of the dissipation rate estimates with different forcing mechanisms such as wind speed $\varepsilon_{SBL,wind}$, buoyancy flux $\varepsilon_{SBL,buoy}$ and bed friction ε_{BBL}. $\varepsilon_{BBL,ADCP}$ correponds to the bottom-generated turbulence estimate based on the ADCP measurements, $\varepsilon_{BBL,ADV}$ – based on the ADV measurements. n is a number of data points (10 min sampling intervals). Total amount of ε_{ADV} is a number of of 10 min time periods with measurements of the ADV dissipation rates.

Dominance of:	Based on the ADCP measurements $\varepsilon_{BBL,ADCP}$	Based on the ADV measurements $\varepsilon_{BBL,ADV}$	Based on the ratio: $\frac{\varepsilon_{BBL,ADV}}{\varepsilon_{SBL,wind}}$ Eq. (11)
$\varepsilon_{SBL,wind}$	n = 2865 42.8%	n = 5291 41.8%	n = 8324 61.7%
$\varepsilon_{SBL,buoy}$	n = 1117 16.7%	n = 1808 14.3%	
ε_{BBL}	n = 2665 39.8%	n = 5387 42.5%	n = 5169 38%
$\varepsilon_{BBL} > \varepsilon_{SBL,wind}$ $\varepsilon_{BBL} > \varepsilon_{SBL,buoy}$ $\varepsilon_{BBL} < \varepsilon_{SBL,wind} + \varepsilon_{SBL,buoy}$	n = 43 0.6%	n = 177 1.4%	
Total amount of data	n = 6690 100%	n = 12663 100%	n = 13493 100%
Total amount of ε_{ADV}	7012		

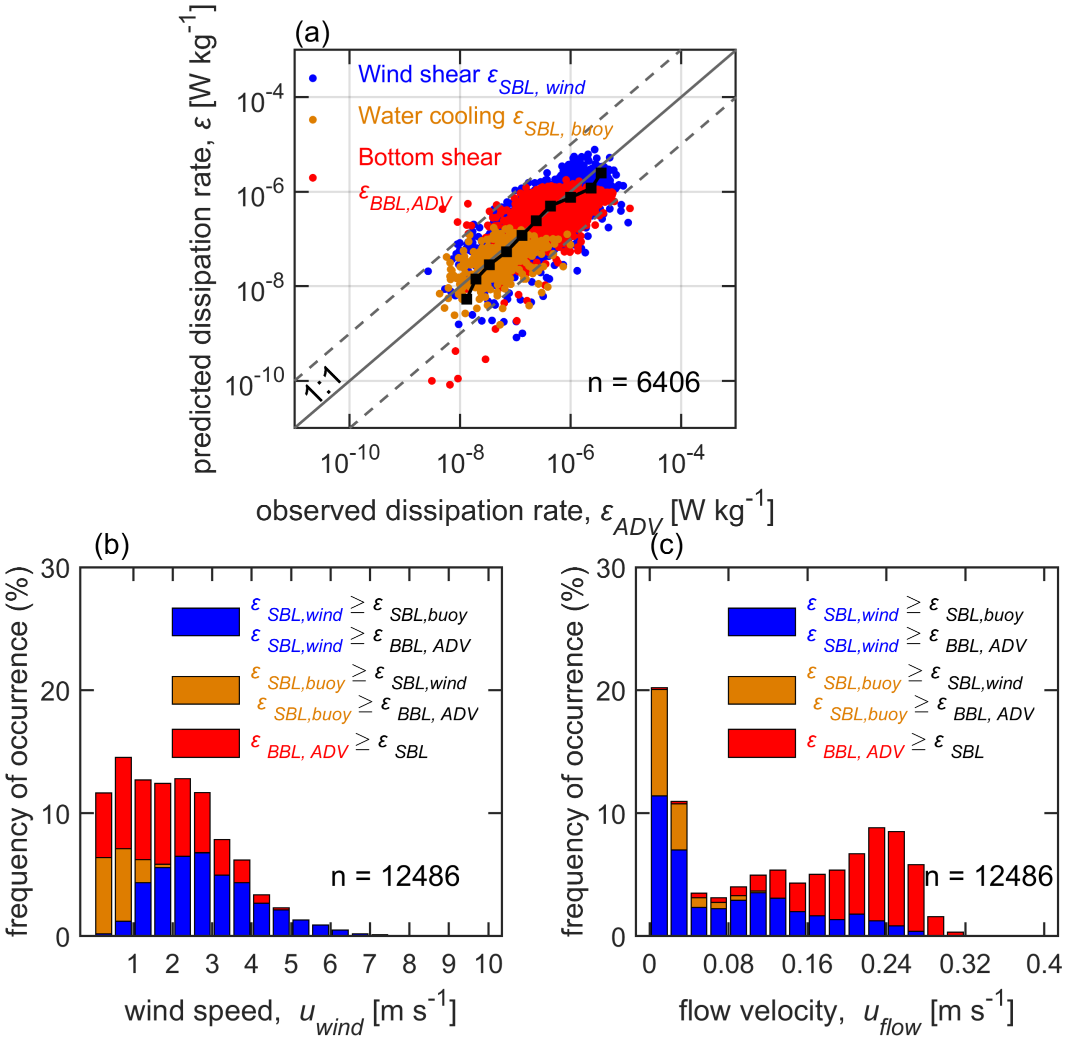

Figure 9. (a) Predicted dissipation rates of turbulent kinetic energy at 0.4 m water depth versus observed values ε_{ADV}. Predictions are based on wind speed $\varepsilon_{SBL,wind}$ and buoyancy flux $\varepsilon_{SBL,buoy}$ if atmospheric forcing was the dominant driver of the near surface turbulence (blue and orange symbols, respectively). The predictions are based on bottom-boundary layer scaling estimated from mean flow velocity $\varepsilon_{BBL,ADV}$ when the bottom-generated turbulence was dominant (red symbols). The black line with square symbols indicates bin-averaged data for all forcing conditions. The solid grey line shows a 1:1 relation, dashed lines represent a one order of magnitude difference. (c) Relative frequency of occurrence of dominant forcing conditions as a function of wind speed and (c) mean flow velocity. n indicates number of data points.

3.5 Effect of water depth

Since near-surface turbulence decays with law of the wall scaling when forced by wind or decreases from the bottom upwards when forced by currents, dominant controls depend on water depth as well as on the distance below the surface at which dissipation rates are measured (Eq. (12)). We addressed this problem in multiple ways. We calculated the critical wind speed $u_{wind,crit}$ for the depth of 0.4 m (ADV measurements). For the water depth at our sampling site of 4.2 m, $u_{wind,crit}$ increased from 1 to 4 m s^{-1} for mean flow velocities between 0.1 and 0.35 m s^{-1}. The critical wind speed increases for decreasing water depth for hypothetical water depths of 1 and 100 m (Figure 10a).

The critical wind speed increases strongly with increasing depth at which wind and bottom generated turbulence are compared. Using Eq.(12), we computed the mean critical wind speed as a function sampling depth below the surface for the range of observed mean flow velocities (at 1 m above the river bed). At the ADV sampling depth (0.4 m below the surface), the mean critical wind is a factor of 3.8 higher compared to $u_{wind,crit}$ estimated for a sampling depth of 8 mm below the surface. This depth corresponds to the Kolmogorov microscale of turbulence, which defines the thickness of a viscous sublayer at the water surface and the depth at which energy dissipation rates are maximal (Lorke & Peeters, 2006).

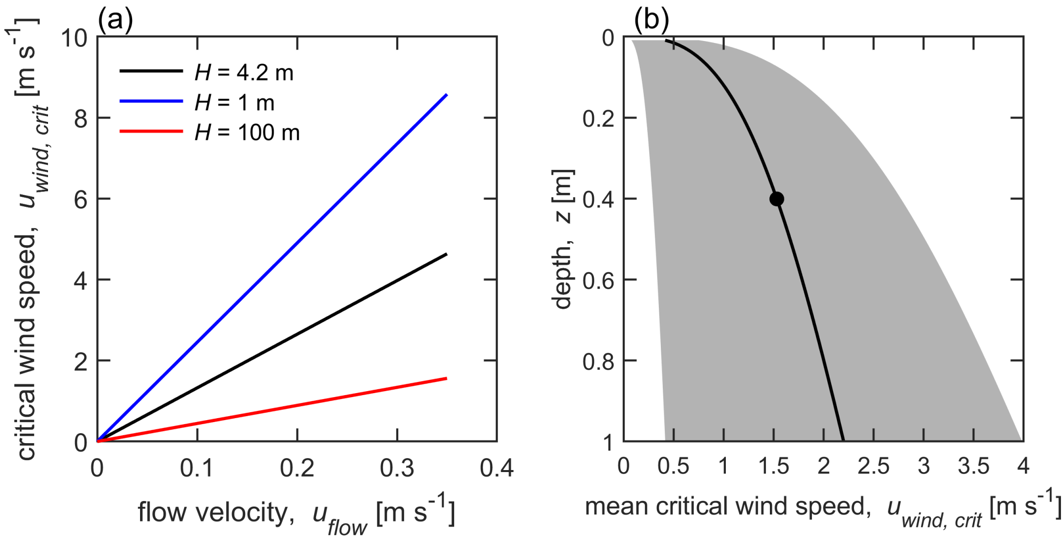

Figure 10. (a) Critical wind speed, above which near-surface turbulence is dominated by wind forcing versus flow velocity for water depths H of 4.2 m (black line), 1 m (blue line), 100 m (red line). The depth at which wind- and bottom generated dissipation rates are compared is 0.4 m (ADV sampling depth). (b) Vertical distribution of mean critical wind speed (black line) calculated for the mean flow velocity observed at 1 m above the bed. The grey area encompasses plus/minus one standard deviation of the mean flow velocity. The black circle marks the depth of 0.4 m for which the critical wind speed in panel a) was estimated . The uppermost depth corresponds to the lower edge of a viscous sublayer (equal to the mean Kolmogorov microscale equal of 8 mm), where dissipation rates are maximal.

3.6 $k - \varepsilon$ model

The numerical 1D $k{-}\varepsilon$ model includes the effects of wind (excluding surface waves), river flow and vertical heat transport on turbulence throughout the water column. In general, results from the $k{-}\varepsilon$ model showed good agreement with observed dissipation rates at 0.4 m water depth ($\rho = 0.6$, $p < 0.05$). The agreement of predictions for dissipation rates calculated from the $k{-}\varepsilon$ model showed comparable agreement with observed dissipation rates as the combined predictions based on bulk atmospheric forcing and mean flow velocity (Figure 11). The model slightly underestimated the dissipation rate by a factor of 0.7. Figure S12 demonstrates an overall performance of the both approaches for cases when the atmospheric forcing or bottom friction was the dominant mechanism in comparison with the $k - \varepsilon$ model results. Dissipation rate simulated by the $k{-}\varepsilon$ model had less agreement with the observed values for the cases when the bottom generated turbulence was dominant (underestimate by a factor of 0.5 by the model in comparison to a factor of 0.9 for the law of the wall scaling (Figure S12a)). For the atmospheric dominant drivers (wind and buoyancy, Figure S12b and Figure S12c, respectively), the $\varepsilon_{k-\varepsilon\ mod}$ had similar agreement with measurements to that of surface similarity scaling. The modeled dissipation rate at 0.1 m depth was on average by a factor of 3.2 higher than one computed at 0.4 m depth.

Water surface water temperature was slightly underestimated by the $k{-}\varepsilon$ model, with a mean difference between modeled and observed temperature was of -0.8 $°C$ (Figure S13). In the model output, short periods of temperature stratification in the river occurred, which were not observed in the measurements. During these periods, strong suppression of dissipation rates was favoured, contributing to the slightly expanded left "tail" of the error distribution in Figure 11 (right). The modeled flow velocity profile (Figure S14) was characterized by the patterns of flow regulation similar to what were observed.

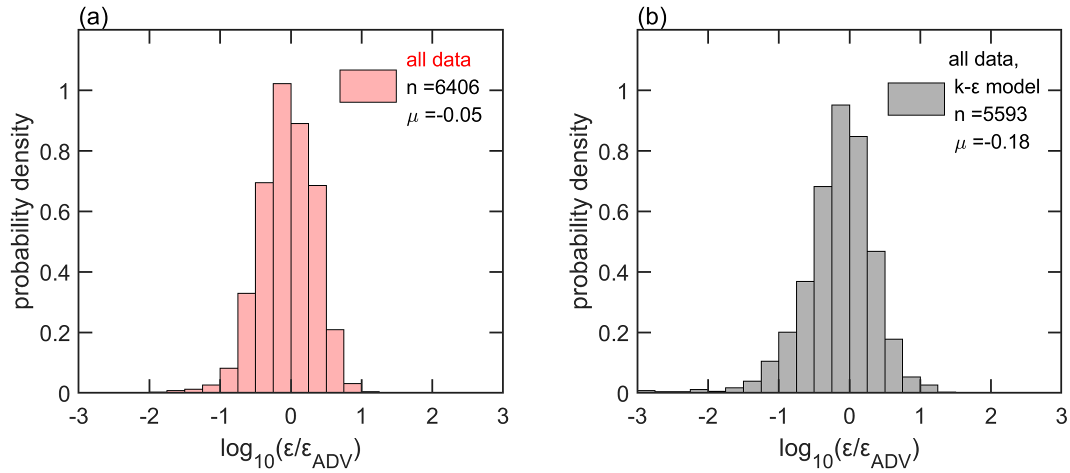

Figure 11. Probability density distributions of the logarithmic ratio of predicted and observed (ε_{ADV}) dissipation rates. (a) Predictions based on mean wind speed and mean flow velocity (combined $\varepsilon_{BBL,ADV}$, ε_{SBL}). (b) Predictions based on the $\varepsilon_{k-\varepsilon\ mod}$. The respective number of data points (n) and mean value (μ) of the logarithm of the ratio are shown the legend.

4 Discussion

4.1 Magnitude, drivers and dynamics of near-surface turbulence

With a Strahler stream order of 5 and a width of approximately 100 m at the study site, the River Kitinen belongs to the class of moderately sized rivers (orders 5–9), which have the greatest area globally, with less area covered by low and high order streams (Downing et al., 2012). Despite their widespread distribution, turbulence measurements in such rivers are rare. In the River Kitinen, dissipation rates of turbulent kinetic energy varied over four orders of magnitude between 10^{-9} and 10^{-5} W kg^{-1} during the ice-free season, with a log-averaged mean value of $4 \cdot 10^{-7}$ W kg^{-1}. This range is comparable to dissipation rates reported from shorter-term observations in a river of similar size in Germany (Lorke et al., 2012). In low-order streams, dissipation rates are consistently higher and can be up to four orders of magnitude higher (Kokic et al., 2018). In tidal estuaries with large river inflows, dissipation rates range from 10^{-6} - 10^{-4} W kg^{-1}, (Zappa et al., 2007; Chickadel et al., 2011). Dissipation rates in the River Kitinen were similar in magnitude to dissipation rates observed in the near-surface layer of lakes, where they typically vary between 10^{-9} and 10^{-5} W kg^{-1} (Wüest & Lorke, 2003; Tedford et al., 2014).

Our measurements are the first to identify the dominant mechanisms forcing near-surface turbulence in the river and their dynamics from minutes to seasonal time scales. Bottom friction and wind shear dominated a similar fraction of the time, 43% and 42% respectively, with turbulence produced by convection only contributing 14% of the time. The temporal dynamics resulted from diel variability in wind speed, buoyancy flux and flow velocity. The latter was strongly affected by flow regulation. The nocturnal reduction of flow velocity due to demand-following hydropower production at the downstream dam, was frequently associated with a transition from the dominance of bottom-generated turbulence to atmospheric forcing and a change of the water body from a lotic to a more lentic-like system.

The contribution of surface waves to the dissipation rates was found to be insignificant, probably due to the small amplitude of the observed waves. Weak thermal stratification, as it was observed during some days, caused a slight suppression of turbulence. Also wind direction relative to the flow was found to have a significant effect near-surface dissipation rates. Nevertheless, these effects were small in comparison to the dynamics of the major drivers.

4.2 Scaling and modeling near-surface turbulence

When atmospheric forcing dominated, near-surface dissipation rates followed a similarity scaling, as it been found in lakes and oceans (Lombardo & Gregg, 1989; Tedford et al., 2014) and could be well predicted from bulk parameters, including wind speed and surface buoyancy flux. Similarly, bottom-generated turbulence followed boundary-layer scaling and its vertical distribution could be well predicted from mean flow velocity after adjusting the bed roughness coefficient. Surprisingly, our observations showed that the vertical decline of bottom-generated turbulence was better described by the law-of-the wall scaling, which is based on the assumption of a constant shear stress, than by Nezu (1977) analysis. The latter has been found to agree well with vertical profiles of dissipation rates measured in smaller rivers (Sukhodolov et al., 1998) and in laboratory flumes (Nezu & Rodi, 1986; Johnson & Cowen, 2017). By combining both approaches for atmospheric and bottom-generated turbulence, we obtained a good prediction of near-surface dissipation rates as a function of bulk atmospheric forcing and mean flow velocity (Figure 9). Although the scatter of individual (10-min based) dissipation rates is large, bin-averaged data revealed an unbiased agreement between prediction and observation. To assess the relative importance of bottom- and wind generated turbulence in rivers of arbitrary depth, we described a new concept in terms of a critical wind speed, which can be derived with the assumption that at some depth the surface boundary layer turbulence is equal to the bottom boundary layer turbulence. We combined both boundary-layer scaling approaches and derived an expression for the critical wind speed as a function of mean flow velocity and water depth (Eq. (12)). For wind speeds exceeding this critical value, near-surface turbulence is expected to be predominantly controlled by wind, in contrast to the predominance of bed friction for wind speed below the the critical value.

In addition to bulk forcing and water depth, the relative importance of wind and bottom-generated turbulence depends strongly on the distance from the surface at which turbulence is observed. Particularly, wind-generated turbulence declines below the water surface and are expected to be highest at the base of the viscous sublayer at the water surface (Lorke & Peeters, 2006). As in most field observations of near-surface turbulence, the distance below the water surface at which turbulence was observed (0.4 m) was limited by the physical dimension of the velocimeter. Spatially resolving measurements of turbulence in the wind-mixed surface layer of a lake using particle image velocimetry, confirmed the existence of a power law decline of dissipation rates, even within the uppermost centimeter of the water column (Wang et al., 2013). The relative importance of wind or flow generated turbulence can be estimated as a function of distance from the water surface using law of the wall scaling (Eq. (12)).

The first prototype of a 1D $k{-}\varepsilon$ model for rivers has been applied to quantify the turbulence throughout the water column. Despite the higher numerical complexity and more comprehensive physics compared to the more simple bulk approaches, the $k-\varepsilon$ model results did not demonstrate substantial improvement in simulating subsurface dissipation rate compared to the similarity-based estimates. The model results were similar to surface similarity scaling when the atmospheric forcing is dominant, because the top boundary condition used in he model is of the same type as the scaling. When the turbulence is dominated by bottom friction, the $k - \varepsilon$ model slightly underestimated the dissipation rates. This result should be interpreted with caution, since the dissipation rate measurements contain significant uncertainties themselves. The discrepancies may result from the well-known knowledge gaps in the construction of optimal two-parameter (e.g. $k{-}\varepsilon$) turbulence closures, namely, specification of stability functions and non-dimensional constants (Mortikov et al., 2019), setup of the surface boundary conditions (Burchard, 2002), inclusion of TKE production by wave-induced motions (Ghantous & Babanin, 2014), to mention a few. Notwithstanding these uncertainties, the $k{-}\varepsilon$ model can be applied to more problems than similarity scaling. As it reproduces the vertical distribution of the turbulent diffusivity in river flow, it can be used for the quantification of vertical transport of water constituents from the sediment to the water surface and eventual emission to the atmosphere. In addition, this model can be applied to the river systems with larger depths. Moreover, it includes a number of physical effects omitted in the bulk approaches, e.g. influence of stable stratification on the flow, which may become more important in low-latitude and slow water flows. Model improvements will need to address the overestimation of solar heating (and corresponding diminishing of turbulence intensity) under low wind and flow speed conditions.

4.3 Implications for gas exchange in regulated rivers

Near-surface turbulence constitutes the primary control on the gas transfer velocity (k) at the air-water interface (Zappa et al., 2007; MacIntyre et al., 2010). k is related to the dissipation rate of turbulent kinetic energy as $k = c_1 (\varepsilon\nu)^{1/4} Sc^{-1/2}$, where Sc is a Schmidt number, c_1 is a scaling parameter (Lamont & Scott, 1970). The mean observed dissipation rate of $4{\cdot}10^{-7}$ W kg^{-1} corresponds to the normalized value of k_{600} (i.e. for $Sc = 600$) of 1.4 m d^{-1} (using $c_1 = 0.5$, (MacIntyre et al., 2010)). This gas transfer velocity is approximately 4 times lower than what has been used for a river with Strahler order of 5 in a global analysis of inland water CO_2 emissions (Raymond et al., 2013). Moreover, the range of variability of dissipation rates spanned four orders of magnitude, which corresponds to temporal variations in k of one order magnitude (0.4 to 3.4 m d^{-1}), with most of the variability occurring at a diel time scale. As also dissolved gas concentration often show diel variations in response to light and temperature, the diel variability of gas fluxes to the atmosphere can be amplified or attenuated, depending on the superposition of both cycles. To the best of our knowledge, direct measurements of gas fluxes from rivers using floating chamber or tracer methods have been conducted during daytime, which can potentially result in a significant bias if these fluxes are assumed to present daily or longer-term mean values in larger-scale estimates. To date, temporal variability of the gas transfer velocity has not resolved in larger-scale models of riverine CO2 emissions, where the gas transfer velocity is typically considered as constant for a stream segment or reach (Raymond et al., 2013; Lauerwald et al., 2015; Magin et al., 2017). Future field observations and modeling efforts are required to analyze the extent, to which diel variability may affect longer-term emission rates.

Alin et al. (2011) suggested a conceptual scheme for the transition of the physical control of gas transfer velocities and fluxes in river systems from the dominance of wind control at the largest in estuaries and river mainstems toward increasing importance of water current velocity and depth at progressively lower stream orders. Our findings confirm this scheme, with the Kitinen River being located in the transition zone, where wind and water currents are of nearly equal importance. Moreover, we provide a quantitative evaluation of this concept, by combining scaling relations for energy dissipation rates generated by wind and water currents as a function of river depth. Our concept of a critical wind speed can be used to separate the two physical forcing regimes and to estimate near-surface dissipation rates and corresponding gas transfer velocities from mean flow velocity or from wind speed.

Our observations revealed that the temporal dynamics of the near-surface turbulence was strongly affected by flow regulation. Demand-following hydropower generation resulted in diel changes of flow velocity from 0.2 - 0.3 m s^{-1} during daytime to some mm s^{-1} at night, changing the physical characteristics of the river from lotic to lentic. As the majority of river systems are affected by flow regulation (Grill et al., 2019), this situation can probably considered as typical. Flow regulation has been shown to decrease flow variability at seasonal scales by homogenization of river discharge (Poff et al., 2007; Long et al., 2019). The effect of flow regulation on shorter, including diel time scales has received comparably less attention. In the regulated river Saar in central Europe, diel variations in flow velocity have been shown to modulate the oxygen flux into the river bed by a factor of two (Lorke et al., 2012). The availability of oxygen in river sediment can be expected to affect mineralization rates and the production of greenhouse gases. Therefore, flow regulation not only modulates near-surface turbulence and, therewith the temporal dynamics of gas fluxes, it may additionally affect the total amount of greenhouse gases emitted from rivers. Despite of its global relevance, this potential implication has not been explored and should be addressed in future studies. Such studies can be based on the scaling approaches or on the 1D $k-\varepsilon$ model, which can be combined with biogeochemcial models for water and sediment as has also been done for lakes at regional scales (e.g., Sabrekov et al. (2017)). These models can be used to explore and to optimize management strategies for flow regulation, that can potentially mitigate adverse effects of river daming on greenhouse gas emissions.

5 Conclusion

The key drivers of near-surface turbulence in a regulated river were analysed based on a comprehensive data set of simultaneous air-side and water-side measurements throughout an ice free season. For the first time, continuous turbulence measurements have been conducted in a large regulated river. Our findings revealed the equal contribution of atmospheric forcing and bottom generated turbulence to the near-surface dissipation rate. After validation of individual scaling approaches, we developed a scaling approach to quantify the dominant forcing mechanism (wind or flow) using a critical value of the wind speed, which depends on the distance from the water surface and on flow depth. Close to the water surface, it is more likely that wind generated turbulence is dominant. Further, direct measurements of the water-side turbulence at depths closer to the water surface in combination with measurements of atmospheric fluxes are required to improve our understanding of the magnitude and controls on air-river gas exchange. As flow regulation proved to be important for the temporal dynamics of the near-surface turbulence, future studies should address the implications of daily and sub-daily flow variations on both the temporal dynamics of fluxes and biogeochemcial cycling in rivers and their sediments.

Appendix A Wave-breaking scaling

Based on measurements in large lakes and in the coastal ocean, Terray et al. (1996); Feddersen et al. (2007) proposed the following scaling for near-surface dissipation rates under breaking surface waves in deep water:

$$\frac{\varepsilon_{wave} H_{sign}}{\alpha(u_{*SBL})^3} = \beta \left(\frac{z}{H_{sign}}\right)^m, \tag{A1}$$

where z is the distance from the water surface, H_{sign} is the significant wave height, $\alpha \sim c_p/u_*^w$ (where c_p is the wave phase speed) is a coefficient which has been found in (Feddersen et al., 2007) equal to 250 for the coastal ocean, $\beta = 0.3$ and $m =$ -2 are the constants. However, measurements conducted by (Wang et al., 2013, 2015) in a large lake suggested scaling constants of $\beta = 0.04$, $m =$ -0.73 within the top layer of water column.

We obtained α and m using a linear regression model for filtered data with wind speed exceeding 1 m s^{-1} and wind directions along the river (Figure S8a). The friction velocity u_{*SBL} was calculated from from mean wind speed. We found $\alpha = 36$ and $m =$ -0.8 which were close to the result in (Wang et al., 2013, 2015). With these values we estimated the dissipation rate including the effect of waves ε_{wave} using Eq. (A2):

$$\varepsilon_{wave} = \beta\alpha(u_{*SBL})^3 \frac{H_{sign}}{z^2}. \tag{A2}$$

Acknowledgments

The data used in this study is available at the Mendeley repository Guseva et al., 2020 [doi: 10.17632/jnbxwyybcn.1]. We are grateful for the scripts provided by Cynthia Bluteau and Galen Charles Egan. We thank Falk Feddersen for consulting us and Alexander Shamanskiy for the mathematical advice. We thank David Bastviken and John Melack for assistance with editing. We are grateful to Daniela Franz, Christoph Bors, Risto Taipale, Anders Lindroth and John Melack for their significant help during field campaign in 2018. We thank Marko Kärkkäinen and Pasi Korpelainen (University of Eastern Finland) for assisting in field work related to the aerial photography of the study area. We thank all people at the field station for organizing the accommodation and food and helping with the instruments and transportation. This work was supported by several funding agencies. Sofya Guseva and Andreas Lorke were supported by the German Research Foundation (DFG) under the grant LO1150/12-1. Mika Aurela was supported by the Academy of Finland (project 296888). Alicia Cortés and Sally MacIntyre were supported by the U.S. N.S.F. 1737411. Eliisa Lotsari was supported by The Department of Geographical and Historical Studies, University of Eastern Finland. Ivan Mammarella and Timo Vesala thank the European Union for supporting the RINGO project funded by the Horizon 2020 Research and Innovation Programme under Grant Agreement 730944. Aki Vähä and Timo Vesala were supported by the University of Helsinki ICOS-Finland. Victor Stepanenko is grateful to Andrey Glazunov and Andrey Debolskiy for advice in setup of simulations with $k-\varepsilon$ model; his work was supported by the Russian Foundation for Basic Research, grant 20-05-00773. Marcus Bo Wallin was supported by the King Carl-Gustaf XVI award for environmental science. Simulations of river turbulence by the $k-\varepsilon$ model have been carried out according to the research program of Moscow Center for Fundamental and Applied Mathematics. The authors declare that they have no conflicts of interest.

References

Åberg, S. C., Korkka-Niemi, K., Rautio, A., Salonen, V.-P., & Åberg, A. K. (2019). Groundwater recharge/discharge patterns and groundwater–surface water interactions in a sedimentary aquifer along the River Kitinen in Sodankylä, northern Finland. *Boreal Environment Research*, *24*, 155–187.

Alin, S. R., de Fátima F. L. Rasera, M., Salimon, C. I., Richey, J. E., Holtgrieve, G. W., Krusche, A. V., & Snidvongs, A. (2011). Physical controls on carbon dioxide transfer velocity and flux in low-gradient river systems and implications for regional carbon budgets. *Journal of Geophysical Research: Biogeosciences*, *116*(G1). doi: 10.1029/2010JG001398

Arcement, G. J., & Schneider, V. R. (1989). *Guide for selecting Manning's roughness coefficients for natural channels and flood plains.* US Government Printing Office Washington, DC.

Aufdenkampe, A. K., Mayorga, E., Raymond, P. A., Melack, J. M., Doney, S. C., Alin, S. R., … Yoo, K. (2011). Riverine coupling of biogeochemical cycles between land, oceans, and atmosphere. *Frontiers in Ecology and the Environment*, *9*(1), 53-60. doi: 10.1890/100014

Bluteau, C. E., Jones, N. L., & Ivey, G. N. (2011). Estimating turbulent kinetic energy dissipation using the inertial subrange method in environmental flows. *Limnology and Oceanography: Methods*, *9*(7), 302-321. doi: 10.4319/lom.2011.9.302

Borges, A. V., Darchambeau, F., Teodoru, C. R., Marwick, T. R., Tamooh, F., Geeraert, N., … Bouillon, S. (2015). Globally significant greenhouse-gas emissions from African inland waters. *Nature Geoscience*, *8*(8), 637–642. doi: 10.1038/ngeo2486

Bormans, M., & Webster, I. T. (1997). A mixing criterion for turbid rivers. *Environmental modelling & software*, *12*(4), 329–333. doi: 10.1016/S1364-8152(97)00032-7

Bouffard, D., & Wüest, A. (2019). Convection in lakes. *Annual Review of Fluid Mechanics*, *51*, 189–215. doi: 10.1146/annurev-fluid-010518-040506

Brumer, S. E., Zappa, C. J., Blomquist, B. W., Fairall, C. W., Cifuentes-Lorenzen, A., Edson, J. B., … Huebert, B. J. (2017). Wave-related Reynolds number parameterizations of CO_2 and DMS transfer velocities. *Geophysical Research Letters*, *44*(19), 9865-9875. doi: 10.1002/2017GL074979

Burchard, H. (2002). *Applied turbulence modelling in marine waters* (Vol. 100). Springer Science & Business Media. doi: 10.1007/3-540-45419-5

Butman, D., & Raymond, P. A. (2011). Significant efflux of carbon dioxide from streams and rivers in the United States. *Nature Geoscience*, *4*(12), 839–842. doi: 10.1038/ngeo1294

Chickadel, C. C., Talke, S. A., Horner-Devine, A. R., & Jessup, A. T. (2011). Infrared-based measurements of velocity, turbulent kinetic energy, and dissipation at the water surface in a tidal river. *IEEE Geoscience and Remote Sensing Letters*, *8*(5), 849–853. doi: 10.1109/LGRS.2011.2125942

Chow, V. T. (1959). *Open-channel hydraulics.* McGraw-Hill Book Co.

Clark, J. F., Wanninkhof, R., Schlosser, P., & Simpson, H. J. (1994). Gas exchange rates in the tidal hudson river using a dual tracer technique. *Tel-*

lus B: Chemical and Physical Meteorology, *46*(4), 274-285. doi: 10.3402/tellusb.v46i4.15802

Cole, J. J., Prairie, Y. T., Caraco, N. F., McDowell, W. H., Tranvik, L. J., Striegl, R. G., … Melack, J. (2007). Plumbing the global carbon cycle: integrating inland waters into the terrestrial carbon budget. *Ecosystems*, *10*(1), 172–185. doi: 10.1007/s10021-006-9013-8

Devol, A. H., Quay, P. D., Richey, J. E., & Martinelli, L. A. (1987). The role of gas exchange in the inorganic carbon, oxygen, and ^{222}Rn budgets of the Amazon River. *Limnology and Oceanography*, *32*(1), 235-248. doi: 10.4319/lo.1987.32.1.0235

Downing, J. A., Cole, J. J., Duarte, C., Middelburg, J. J., Melack, J. M., Prairie, Y. T., … Tranvik, L. J. (2012). Global abundance and size distribution of streams and rivers. *Inland waters*, *2*(4), 229–236. doi: 10.5268/IW-2.4.502

Feddersen, F., Trowbridge, J. H., & Williams III, A. (2007). Vertical structure of dissipation in the nearshore. *Journal of Physical Oceanography*, *37*(7), 1764–1777. doi: 10.1175/JPO3098.1

Gerbi, G. P., Trowbridge, J. H., Terray, E. A., Plueddemann, A. J., & Kukulka, T. (2009). Observations of turbulence in the ocean surface boundary layer: Energetics and transport. *Journal of Physical Oceanography*, *39*(5), 1077–1096. doi: 10.1175/2008JPO4044.1

Ghantous, M., & Babanin, A. (2014). One-dimensional modelling of upper ocean mixing by turbulence due to wave orbital motion. *Nonlinear Processes Geophys*, *21*(1), 325–338. doi: 10.5194/npg-21-325-2014

Goring, D. G., & Nikora, V. I. (2002). Despiking Acoustic Doppler Velocimeter Data. *Journal of Hydraulic Engineering*, *128*(1), 117–126. doi: 10.1061/(ASCE)0733-9429(2002)128:1(117)

Grill, G., Lehner, B., Thieme, M., Geenen, B., Tickner, D., Antonelli, F., … Zarfl, C. (2019). Mapping the world's free-flowing rivers. *Nature*, *569*(7755), 215. doi: 10.1038/s41586-019-1111-9

Hall Jr., R. O., & Madinger, H. L. (2018). Use of argon to measure gas exchange in turbulent mountain streams. *Biogeosciences*, *15*(10), 3085–3092. doi: 10.5194/bg-15-3085-2018

Hicks, B. (1972). Some evaluations of drag and bulk transfer coefficients over water bodies of different sizes. *Boundary-Layer Meteorology*, *3*(2), 201–213. doi: 10.1007/BF02033919

Holtgrieve, G. W., Schindler, D. E., Branch, T. A., & A'mar, Z. T. (2010). Simultaneous quantification of aquatic ecosystem metabolism and reaeration using a Bayesian statistical model of oxygen dynamics. *Limnology and Oceanography*, *55*(3), 1047-1063. doi: 10.4319/lo.2010.55.3.1047

Johnson, E. D., & Cowen, E. A. (2017). Estimating bed shear stress from remotely measured surface turbulent dissipation fields in open channel flows. *Water Resources Research*, *53*(3), 1982-1996. doi: 10.1002/2016WR018898

Katul, G., & Liu, H. (2017). Multiple mechanisms generate a universal scaling with dissipation for the air-water gas transfer velocity. *Geophysical Research Letters*, *44*(4), 1892-1898. doi: 10.1002/2016GL072256

Kokic, J., Sahlée, E., Sobek, S., Vachon, D., & Wallin, M. B. (2018). High spatial variability of gas transfer velocity in streams revealed by turbulence measurements. *Inland Waters*, *8*(4), 461–473. doi: 10.1080/20442041.2018.1500228

Krause, F. (2011). River management. Technological challenge or conceptual illusion? Salmon weirs and hydroelectric dams on the Kemi River in Northern Finland. In *Implementing environmental and resource management* (pp. 229–248). Springer.

Lamont, J. C., & Scott, D. (1970). An eddy cell model of mass transfer into the surface of a turbulent liquid. *AIChE Journal*, *16*(4), 513–519. doi: 10.1002/aic.690160403

Lauerwald, R., Laruelle, G. G., Hartmann, J., Ciais, P., & Regnier, P. A. (2015). Spatial patterns in CO_2 evasion from the global river network. *Global Biogeochemical Cycles*, *29*(5), 534-554. doi: 10.1002/2014GB004941

Lehner, B., Verdin, K., & Jarvis, A. (2008). New global hydrography derived from spaceborne elevation data. *Eos, Transactions American Geophysical Union*, *89*(10), 93-94. doi: 10.1029/2008EO100001

Lombardo, C. P., & Gregg, M. C. (1989). Similarity scaling of viscous and thermal dissipation in a convecting surface boundary layer. *Journal of Geophysical Research: Oceans*, *94*(C5), 6273-6284. doi: 10.1029/JC094iC05p06273

Long, L., Ji, D., Liu, D., Yang, Z., & Lorke, A. (2019). Effect of Cascading Reservoirs on the Flow Variation and Thermal Regime in the Lower Reaches of the Jinsha River. *Water*, *11*(5), 1008.

Lorke, A., & MacIntyre, S. (2009). The benthic boundary layer (in rivers, lakes, and reservoirs). In G. E. Likens (Ed.), *Encyclopedia of inland waters* (p. 505 - 514). Oxford: Academic Press. doi: 10.1016/B978-012370626-3.00079-X

Lorke, A., McGinnis, D. F., Maeck, A., & Fischer, H. (2012). Effect of ship locking on sediment oxygen uptake in impounded rivers. *Water Resources Research*, *48*(12). doi: 10.1029/2012WR012483

Lorke, A., & Peeters, F. (2006). Toward a Unified Scaling Relation for Interfacial Fluxes. *Journal of Physical Oceanography*, *36*(5), 955-961. doi: 10.1175/JPO2903.1

Lorke, A., & Wüest, A. (2005). Application of coherent ADCP for turbulence measurements in the bottom boundary layer. *Journal of Atmospheric and Oceanic Technology*, *22*(11), 1821–1828. doi: 10.1175/JTECH1813.1

MacIntyre, S., Jonsson, A., Jansson, M., Aberg, J., Turney, D. E., & Miller, S. D. (2010). Buoyancy flux, turbulence, and the gas transfer coefficient in a stratified lake. *Geophysical Research Letters*, *37*(24). doi: 10.1029/2010GL044164

MacIntyre, S., Romero, J. R., & Kling, G. W. (2002). Spatial-temporal variability in surface layer deepening and lateral advection in an embayment of Lake Victoria, East Africa. *Limnology and Oceanography*, *47*(3), 656-671. doi: 10.4319/lo.2002.47.3.0656

MacIntyre, S., Romero, J. R., Silsbe, G. M., & Emery, B. M. (2014). Stratification and horizontal exchange in Lake Victoria, East Africa. *Limnology and Oceanography*, *59*(6), 1805-1838. doi: 10.4319/lo.2014.59.6.1805

Magin, K., Somlai-Haase, C., Schäfer, R. B., & Lorke, A. (2017). Regional-scale lateral carbon transport and CO_2 evasion in temperate stream catchments. *Biogeosciences*, *14*(21), 5003–5014. doi: 10.5194/bg-14-5003-2017

McMillen, R. T. (1988). An eddy correlation technique with extended applicability to non-simple terrain. *Boundary-Layer Meteorology*, *43*(3), 231–245. doi: 10.1007/BF00128405

Mortikov, E., Glazunov, A., Debolskiy, A., Lykosov, V., & Zilitinkevich, S. (2019). Modeling of the dissipation rate of turbulent kinetic energy. *Doklady Earth Sciences*, *489*(2), 1440–1443. doi: 10.1134/S1028334X19120067

Moum, J. N., Gregg, M. C., Lien, R. C., & Carr, M. E. (1995). Comparison of turbulence kinetic energy dissipation rate estimates from two ocean microstructure profilers. *Journal of Atmospheric and Oceanic Technology*, *12*(2), 346-366. doi: 10.1175/1520-0426(1995)012⟨0346:COTKED⟩2.0.CO;2

Natchimuthu, S., Wallin, M. B., Klemedtsson, L., & Bastviken, D. (2017). Spatio-temporal patterns of stream methane and carbon dioxide emissions in a hemiboreal catchment in Southwest Sweden. *Scientific reports*, *7*, 39729. doi: 10.1038/srep39729

Neumann, G., & Pierson, W. (1966). *Principles of physical oceanography.* Prentice-Hall.

Nezu, I. (1977). *Turbulent structure in open-channel flows* (PhD dissertation). Kyoto University, Japan.

Nezu, I., & Rodi, W. (1986). Open-channel flow measurements with a laser Doppler anemometer. *Journal of Hydraulic Engineering*, *112*(5), 335–355. doi: 10.1061/(ASCE)0733-9429(1986)112:5(335)

Nortek, A. S. (2015). The Comprehensive Manual [Computer software manual]. Retrieved from `http://www.nortek.no/en/support/manuals`

Ott, M. W. (2002). An improvement in the calculation of ADCP velocities. *Journal of Atmospheric and Oceanic Technology*, *19*(10), 1738–1741. doi: 10.1175/1520-0426(2002)019⟨1738:AIITCO⟩2.0.CO;2

Poff, N. L., Olden, J. D., Merritt, D. M., & Pepin, D. M. (2007). Homogenization of regional river dynamics by dams and global biodiversity implications. *Proceedings of the National Academy of Sciences*, *104*(14), 5732–5737. doi: 10.1073/pnas.0609812104

Pope, S. B. (2000). *Turbulent flows.* Cambridge University Press. doi: 10.1017/CBO9780511840531

Raymond, P. A., Hartmann, J., Lauerwald, R., Sobek, S., McDonald, C., Hoover, M., ... Guth, P. (2013). Global carbon dioxide emissions from inland waters. *Nature*, *503*(7476), 355. doi: 10.1038/nature12760

Raymond, P. A., Zappa, C. J., Butman, D., Bott, T. L., Potter, J., Mulholland, P., ... Newbold, D. (2012). Scaling the gas transfer velocity and hydraulic geometry in streams and small rivers. *Limnology and Oceanography: Fluids and Environments*, *2*(1), 41–53. doi: 10.1215/21573689-1597669

Richey, J. E., Melack, J. M., Aufdenkampe, A. K., Ballester, V. M., & Hess, L. L. (2002). Outgassing from Amazonian rivers and wetlands as a large tropical source of atmospheric CO_2. *Nature*, *416*(6881), 617–620. doi: 10.1038/416617a

Sabrekov, A. F., Runkle, B. R. K., Glagolev, M. V., Terentieva, I. E., Stepanenko, V. M., Kotsyurbenko, O. R., ... Pokrovsky, O. S. (2017). Variability in methane emissions from west Siberia's shallow boreal lakes on a regional scale and its environmental controls. *Biogeosciences*, *14*(15), 3715–3742. doi: 10.5194/bg-14-3715-2017

Stepanenko, V., Mammarella, I., Ojala, A., Miettinen, H., Lykosov, V., & Vesala, T. (2016, may). LAKE 2.0: a model for temperature, methane, carbon dioxide and oxygen dynamics in lakes. *Geoscientific Model Development*, *9*(5), 1977–2006. Retrieved from `http://www.geosci-model-dev.net/9/1977/2016/` doi: 10.5194/gmd-9-1977-2016

Sukhodolov, A., Thiele, M., & Bungartz, H. (1998). Turbulence structure in a river reach with sand bed. *Water Resources Research*, *34*(5), 1317–1334. doi: 10.1029/98WR00269

Tedford, E. W., MacIntyre, S., Miller, S. D., & Czikowsky, M. J. (2014). Similarity scaling of turbulence in a temperate lake during fall cooling. *Journal of Geophysical Research: Oceans*, *119*(8), 4689–4713. doi: 10.1002/2014JC010135

Terray, E., Donelan, M., Agrawal, Y., Drennan, W. M., Kahma, K., Williams, A. J., ... Kitaigorodskii, S. (1996). Estimates of kinetic energy dissipation under breaking waves. *J. Phys. Oceanogr.*, *26*(5), 792–807. doi: 10.1175/1520-0485(1996)026⟨0792:EOKEDU⟩2.0.CO;2

Tranvik, L. J., Downing, J. A., Cotner, J. B., Loiselle, S. A., Striegl, R. G., Ballatore, T. J., ... Weyhenmeyer, G. A. (2009). Lakes and reservoirs as regulators of carbon cycling and climate. *Limnology and Oceanography*, *54*(6part2), 2298-2314. doi: 10.4319/lo.2009.54.6_part_2.2298

Ulseth, A. J., Hall, R. O., Canadell, M. B., Madinger, H. L., Niayifar, A., & Battin, T. J. (2019). Distinct air–water gas exchange regimes in low-and high-energy streams. *Nature Geoscience*, *12*(4), 259. doi: 10.1038/s41561-019-0324-8

Wahl, T. L. (2003). Discussion of "Despiking Acoustic Doppler Velocimeter Data" by Derek G. Goring and Vladimir I. Nikora. *Journal of Hydraulic Engineering*, *129*(6), 484–487. doi: 10.1061/(ASCE)0733-9429(2003)129:6(484)

Wallin, M. B., Campeau, A., Audet, J., Bastviken, D., Bishop, K., Kokic, J., ... others (2018). Carbon dioxide and methane emissions of Swedish low-order streams—a national estimate and lessons learnt from more than a decade of observations. *Limnology and Oceanography Letters*, *3*(3), 156–167. doi: 10.1002/lol2.10061

Wang, B., Liao, Q., Fillingham, J. H., & Bootsma, H. A. (2015). On the coefficients of small eddy and surface divergence models for the air-water gas transfer velocity. *Journal of Geophysical Research: Oceans*, *120*(3), 2129–2146. doi: 10.1002/2014JC010253

Wang, B., Liao, Q., Xiao, J., & Bootsma, H. A. (2013). A free-floating PIV system: Measurements of small-scale turbulence under the wind wave surface. *Journal of Atmospheric and Oceanic Technology*, *30*(7), 1494–1510. doi: 10.1175/JTECH-D-12-00092.1

Wüest, A., & Lorke, A. (2003). Small-scale hydrodynamics in lakes. *Annual Review of fluid mechanics*, *35*(1), 373–412. doi: 10.1146/annurev.fluid.35.101101.161220

Zappa, C. J., McGillis, W. R., Raymond, P. A., Edson, J. B., Hintsa, E. J., Zemmelink, H. J., ... Ho, D. T. (2007). Environmental turbulent mixing controls on air-water gas exchange in marine and aquatic systems. *Geophysical Research Letters*, *34*(10). doi: 10.1029/2006GL028790

Supporting Information for "Variable physical drivers of near-surface turbulence in a regulated river"

S. Guseva[1], M. Aurela[2], A. Cortés[3], R. Kivi[4], E. Lotsari[5,6], S. MacIntyre[3], I. Mammarella[7], A. Ojala[8,9,10], V. Stepanenko[11,12], P. Uotila[7], A. Vähä[7], T. Vesala[7,9], M. B. Wallin[13,14] and A. Lorke[1]

[1]Institute for Environmental Sciences, University of Koblenz-Landau, Landau, Germany

[2]Climate Research Programme, Finnish Meteorological Institute, Helsinki, Finland

[3]Earth Research Institute, University of California, Santa Barbara, California

[4]Space and Earth Observation Centre, Finnish Meteorological Institute, Sodankylä, Finland

[5]Department of Geographical and Historical Studies, University of Eastern Finland, Joensuu, Finland

[6]Department of Geography and Geology, University of Turku, Turku, Finland

[7]Institute of Atmospheric and Earth System Research (INAR)/ Physics, University of Helsinki, Helsinki, Finland

[8]Ecosystems and Environment Research Programme, Faculty of Biological and Environmental Sciences, University of Helsinki, Helsinki, Finland

[9]Institute for Atmosphere and Earth System Research/Forest Sciences, Faculty of Agriculture and Forestry, University of Helsinki, Helsinki, Finland

[10]Helsinki Institute of Sustainability Science (HELSUS), Faculty of Biological and Environmental Sciences University of Helsinki, Helsinki, Finland

[11]Laboratory for Supercomputer Modeling of Climate System Processes, Research Computing Center, Lomonosov Moscow State University, Moscow, Russia

[12]Department of Meteorology and Climatology, Faculty of Geography, Lomonosov Moscow State University, Moscow, Russia

[13]Department of Earth Sciences: Air, Water and Landscape, Uppsala University, Uppsala, Sweden

[14]Department of Aquatic Sciences and Assessment, Swedish University of Agricultural Sciences, Uppsala, Sweden

Contents of this file

Introduction

In SI we add necessary figures and sections which are not included to the main text. Texts S1-S3 and Figures S1-S3 include the details of computation of the near-surface dissipation rate for two instruments: Acoustic Doppler Velocimeter (ADV) and Acoustic Doppler Current Profiler (ADCP). Text S4 provides the main equations for the one-dimensional $k - \varepsilon$ model used for computation of flow characteristics and turbulence. Text S5 and Figure S7 introduces the procedure of the logarithmic bin-averaging of the data scatter. Figure S4-S6 include additional time series of air and water temperature, relative humidity, water level fluctuation and significant wave height. Figure S8 explores the influence of the surface waves on the near-surface dissipation rate (see additional information in Appendix A). Figure S9, Tables S1-S2 provide detailed information about the overall performance of the bottom boundary layer scaling using the ADCP measurements. Figures S10-S11 explore the possible influence of the stratification and wind direction on the different approaches used for computation of the near-surface dissipation rate. Figures S12-S14 provide additional information of the one-dimensional $k - \varepsilon$ model performance: comparison with different approaches for estimation of the near-surface turbulence, modeling the temperature and flow velocity profiles. We believe this supplementary will provide a complete view of our manuscript.

Text S1. Optimization procedure for identification of the low frequency of the inertial subrange for ADV

The lower frequency limit ω_{low} (or we use k_{low} in the space domain in this case) of the spectral range for inertial subrange (IS) was found by solving the following optimization problem:

$$k_{low} = \arg\min_{\widetilde{k}\in\mathbb{R}} ||E_{33}(k) - \varepsilon_{fit}^{2/3}(\widetilde{k})E_{fit}(k,\widetilde{k})||, \quad (1)$$

where

$$E_{fit}(k,\widetilde{k}) = \begin{cases} const = \widetilde{k}^{-5/3}A_3\alpha_K, & \text{if } k < \widetilde{k}, \\ slope(-5/3) = k^{-5/3}A_3\alpha_K, & \text{if } k \geqslant \widetilde{k}, \end{cases} \quad (2)$$

and

$$\varepsilon_{fit}(\widetilde{k}) = \left(10^{\left\langle \log_{10}(E_{33}(k)/E_{fit}(k,\widetilde{k}))\right\rangle}\right)^{3/2}. \quad (3)$$

Here, $\varepsilon_{fit}^{2/3}(\widetilde{k})E_{fit}(k,\widetilde{k})$ is a fit consisting of an initial constant part and a -5/3 slope. The transition between the parts is defined by the breakpoint $\widetilde{k}$. The cost function $E_{33}(k) - \varepsilon_{fit}^{2/3}(\widetilde{k})E_{fit}(k,\widetilde{k})$ depends smoothly on $\widetilde{k}$ and measures the difference between the fit and the spectrum E_{33}. By minimizing the cost function, we obtain on optimal breakpoint k which defines the lower boundary of the IS. The optimization problem (1–3) is a general nonlinear optimization problem, and we solve it using the Matlab gradient-based optimization solver $fmincon$ (Figure S1). Here, the angled brackets denote averaging over all wave numbers k for which the inertial subrange fit was applied.

Text S2. Identification of the lower and upper frequencies of the inertial subrange for ADCP

The lower frequency limit for inertial subrange fitting (see Eq. 1 in the main text) was defined empirically by considering different flow and wind speed conditions (low, medium, high). We assumed the largest size of eddies l, which corresponds to the lower frequency limit of the inertial subrange, scales with the distance from the surface. It turned out that the eddy size varied between $l = 4 - 4.5$ m in the absence of a wave peak (we calculated $\omega_{low} = 2\pi\overline{u}_{flow}/l$, or depending on mean flow speed $\omega_{low} \sim 0.002$ - 0.3 rad s^{-1}). In the presence of waves, it varied between 3 – 4.5 m. The upper frequency limit for inertial subrange fitting (ω_{low}) was defined empirically for all cases mentioned above in situations where there are no waves. In the presence of surface waves, it was defined as a frequency where function $f = S \cdot \omega$ had a minimum value on the interval $0.1 \leqslant \omega_{up} \leqslant 0.3$ rad s^{-1} for the situations when the flow velocity was low ($\overline{u}_{flow} \leqslant 0.1$ m s^{-1}) and on the interval $0.3 \leqslant \omega_{up} \leqslant 1$ rad s^{-1} in all the left cases.

Text S3. Comparison of dissipation rates from ADV and ADCP

We compare the dissipation rates estimated from single-point velocity measurements near the water surface (ADV, 0.4 m water depth) with those estimated from a bottom-mounted profiler (ADCP for the same depth (Figure S3). There was general agreement between both dissipation rates, however, there was a large scatter among individual measurements (10 min resolution) and partially also a systematic bias at high dissipation rates ($> 10^{-6}$ W kg^{-1}). The bias can be removed by applying optional quality assurance (QA) criterion (length of the observed inertial subrange, Figure S3b, c, d). While mainly high dissipation rates were removed by sharpening the QA criteria, the number of valid data points was strongly reduced (e.g. from number of data points $n = 4425$ for the data without QA to $n = 469$ for data with all QA criteria applied, Figure S3d).

Text S4. The equations of the one-dimensional $k - \varepsilon$ model

$$\frac{\partial \overline{u}}{\partial t} = -g\overline{\frac{\partial h_s}{\partial x}} + \frac{\partial}{\partial z}\left((\nu_m + \nu_t)\frac{\partial \overline{u}}{\partial z}\right), \tag{4}$$

$$\frac{\partial \overline{v}}{\partial t} = \frac{\partial}{\partial z}\left((\nu_m + \nu_t)\frac{\partial \overline{v}}{\partial z}\right), \tag{5}$$

$$\frac{\partial \overline{T}}{\partial t} = \frac{\partial}{\partial z}\left((k_m + k_t)\frac{\partial \overline{T}}{\partial z}\right) - \frac{\partial \overline{S}}{\partial z}, \tag{6}$$

where $\overline{(...)}$ stands for horizontal averaging, u, v are longitudinal and transversal velocity components, respectively, T is water temperature, ν is viscosity coefficient, k is thermal conductivity coefficient, subscripts m and t denote molecular and turbulent counterparts, h_s is free water surface height, S – kinematic radiation flux, g is the modulus of acceleration due to gravity, x is longitudinal coordinate, z – vertical coordinate directed downwards. The Coriolis force is traditionally neglected for rivers given a small width of rivers compared to barotropic Rossby radius of deformation. To close the system, equations for turbulent kinetic energy k (TKE) and its dissipation rate ε are added (Stepanenko et al., 2016).

Text S5. Logarithmic bin average of the data

Estimates of dissipation rates of turbulent kinetic energy in stationary turbulence are expected to be log-normally distributed (Baker & Gibson, 1987). For the comparison of dissipation rate estimates from measurements and predictions, we calculated bin-averages using the following procedure:

Data $\longrightarrow$ Log$_{10}$ transformation of the data $\longrightarrow$ Data rotation by α =-45° $\longrightarrow$Data splitting into bins along the 1:1 line (which coincides with the x-axis) $\longrightarrow$ Data averaging in each bin $\longrightarrow$ Data rotation by α =45° $\longrightarrow$ Reversing the logarithmic transformation

The procedure is illustrated in Figure S7. Data rotation was implemented by a right matrix multiplication $D \to A \cdot D$, where A is a 2×2 rotation matrix and D is a $2 \times n$ matrix consisting of rows data$_x$ and data$_y$:

$$A = \begin{pmatrix} \cos\alpha & -\sin\alpha \\ \sin\alpha & \cos\alpha \end{pmatrix}, \quad D = \begin{pmatrix} \mathrm{data}_x \\ \mathrm{data}_y \end{pmatrix}. \tag{7}$$

References

Arcement, G. J., & Schneider, V. R. (1989). *Guide for selecting Manning's roughness coefficients for natural channels and flood plains.* US Government Printing Office Washington, DC.

Baker, M. A., & Gibson, C. H. (1987). Sampling Turbulence in the Stratified Ocean: Statistical Consequences of Strong Intermittency. *Journal of Physical Oceanography*, *17*(10), 1817-1836. doi: 10.1175/1520-0485(1987)017⟨1817:STITSO⟩2.0.CO;2

Chow, V. T. (1959). *Open-channel hydraulics.* McGraw-Hill Book Co.

Feddersen, F., Trowbridge, J. H., & Williams III, A. (2007). Vertical structure of dissipation in the nearshore. *Journal of Physical Oceanography*, *37*(7), 1764–1777. doi: 10.1175/JPO3098.1

Nezu, I. (1977). *Turbulent structure in open-channel flows* (PhD dissertation). Kyoto University, Japan.

Siddiqui, M. K., & Loewen, M. R. (2007). Characteristics of the wind drift layer and microscale breaking waves. *Journal of Fluid Mechanics*, *573*, 417–456. doi: 10.1017/S0022112006003892

Stepanenko, V., Mammarella, I., Ojala, A., Miettinen, H., Lykosov, V., & Vesala, T. (2016, may). LAKE 2.0: a model for temperature, methane, carbon dioxide and oxygen dynamics in lakes. *Geoscientific Model Development*, *9*(5), 1977–2006. Retrieved from `http://www.geosci-model-dev.net/9/1977/2016/` doi: 10.5194/gmd-9-1977-2016

Tominaga, A., & Sakaki, T. (2010). Evaluation of bed shear stress from velocity measurements in gravel-bed river with local non-uniformity. In A. Dittrich (Ed.), *River flow* (pp. 187–194). A.A. Balkema, Rotterdam.

Wang, B., Liao, Q., Xiao, J., & Bootsma, H. A. (2013). A free-floating PIV system: Measurements of small-scale turbulence under the wind wave surface. *Journal of Atmospheric and Oceanic Technology*, *30*(7), 1494–1510. doi: 10.1175/JTECH-D-12-00092.1

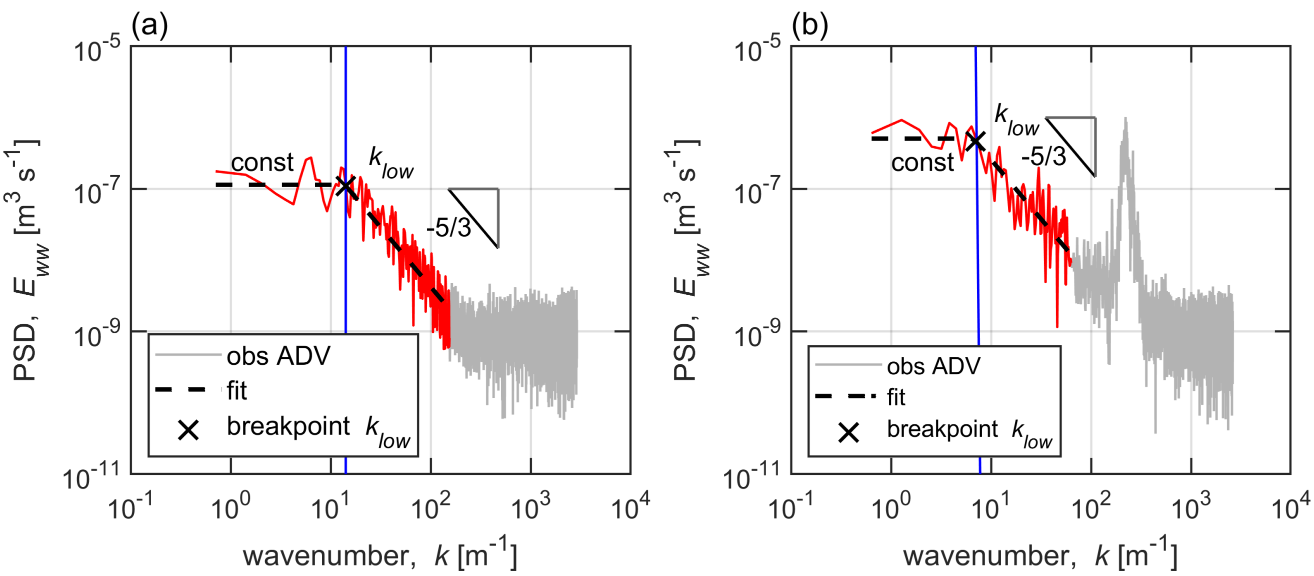

Figure S1. Typical wave number spectra (power spectral density (PSD)$E_{ww}(k)$, grey lines) of vertical velocity fluctuations observed within a 10 min period of ADV measurements: (a) without surface waves and (b) with surface waves. The part of the spectrum marked by red color was selected for spectral fitting by applying a high-frequency cut-off (see Section 2.4.1). The lower wave number limit for inertial subrange fitting (k_{low}, marked by the black cross symbol and blue vertical line) was obtained, by solving a linear optimization problem (see Text S2). The procedure seeks the breakpoint between the spectral slope equal to 1 (constant PSD) and -5/3 slope.

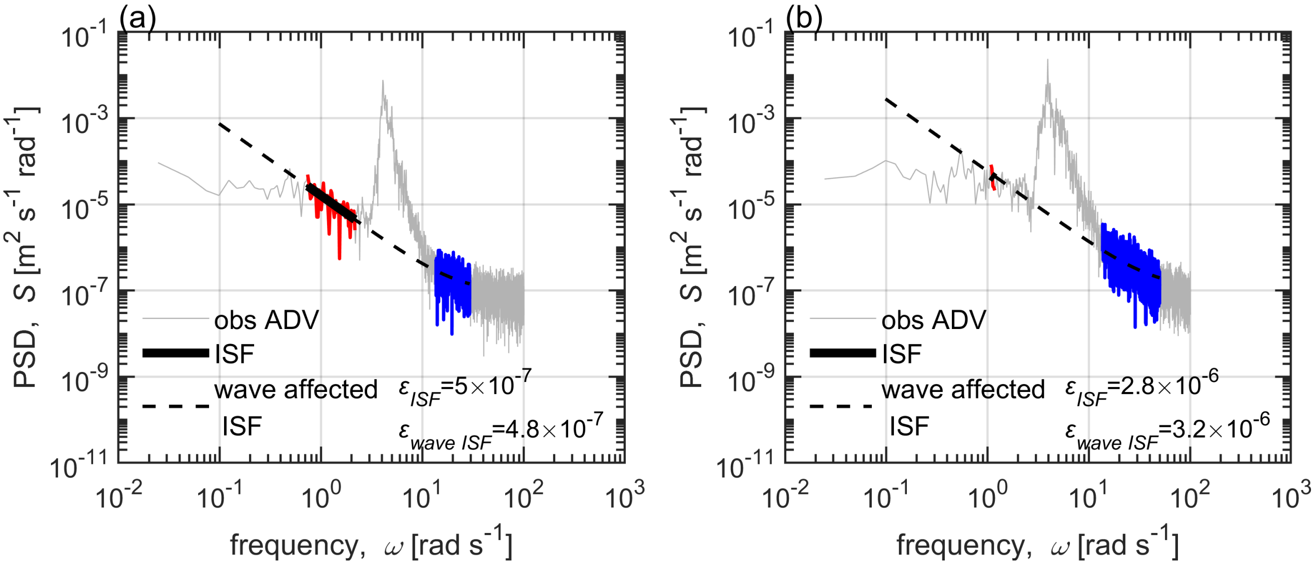

Figure S2. Typical frequency spectra (power spectral density PSD, grey lines) of vertical velocity fluctuations at 0.4 m water depth for time periods with surface waves. The frequency range marked by blue color was used for spectral fitting of the wave affected inertial subrange method (Eq. 2, see Section 2.4.1) and the range marked red for the regular inertial subrange fit (Eq. 1, see Section 2.4.1). The fit obtained from the latter is shown as a thick black line, while the extrapolated fit from the wave-affected part is shown as a black dashed line. (a) Spectrum with long inertial subrange with dissipation rate estimated from both sides of the wave peak; (b) spectrum with a short inertial subrange at frequencies before the wave peak. Whenever a sufficiently long (more than a third of the decade) inertial subrange existed to the left of the peak, we used the estimate of the dissipation rate using the regular inertial subrange fitting. Otherwise, we used the wave affected inertial subrange method. The final dissipation rate consisted of combination of both estimates.

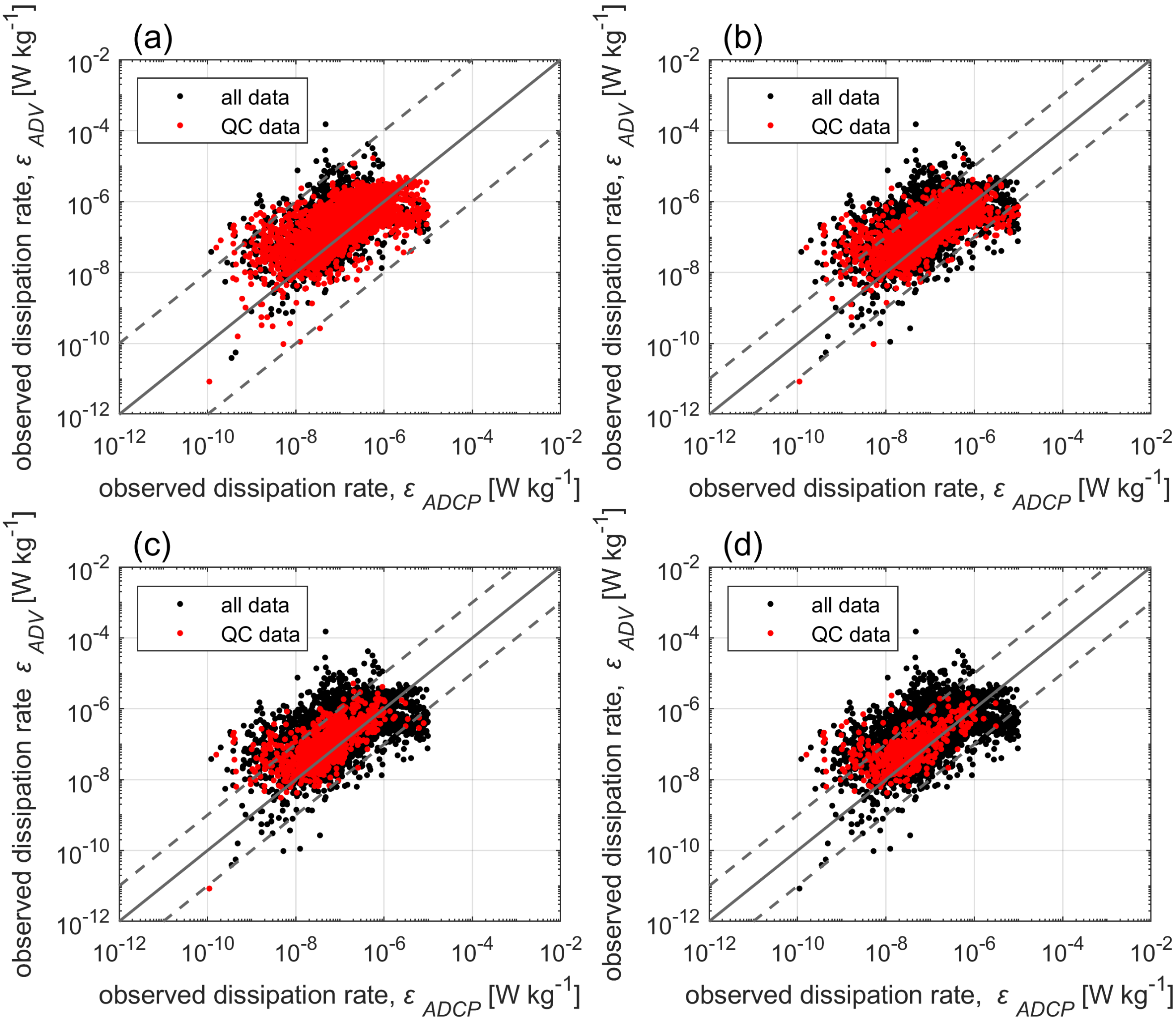

Figure S3. Observed dissipation rate from ADV ε_{ADV} at 0.4 m depth vs observed dissipation rate from ADCP ε_{ADCP} (at $\sim$ 0.4 m) obtained from inertial subrange fitting (see Eq. 1, see Section 2.4.1). For all data (black symbols) no quality check (QC) criteria were applied (number of the data points $n = 4425$). For (a) the following QC criteria were applied: criterion of frozen turbulence, coefficient of determination (red symbols, $n = 2618$), the solid grey line (also in (b)-(d)) shows a 1:1 relation between both dissipation rates and two dashed lines indicate differences of two orders of magnitude; (b) optional criterion for the length (frequency range) of the inertial subrange more than 1/5 of decade ($n = 1496$), two dashed lines indicate differences of one order of magnitude (also in (c), (d)); (c) more than 1/3 of decade ($n = 775$); (d) more than 1/2 of decade ($n = 469$).

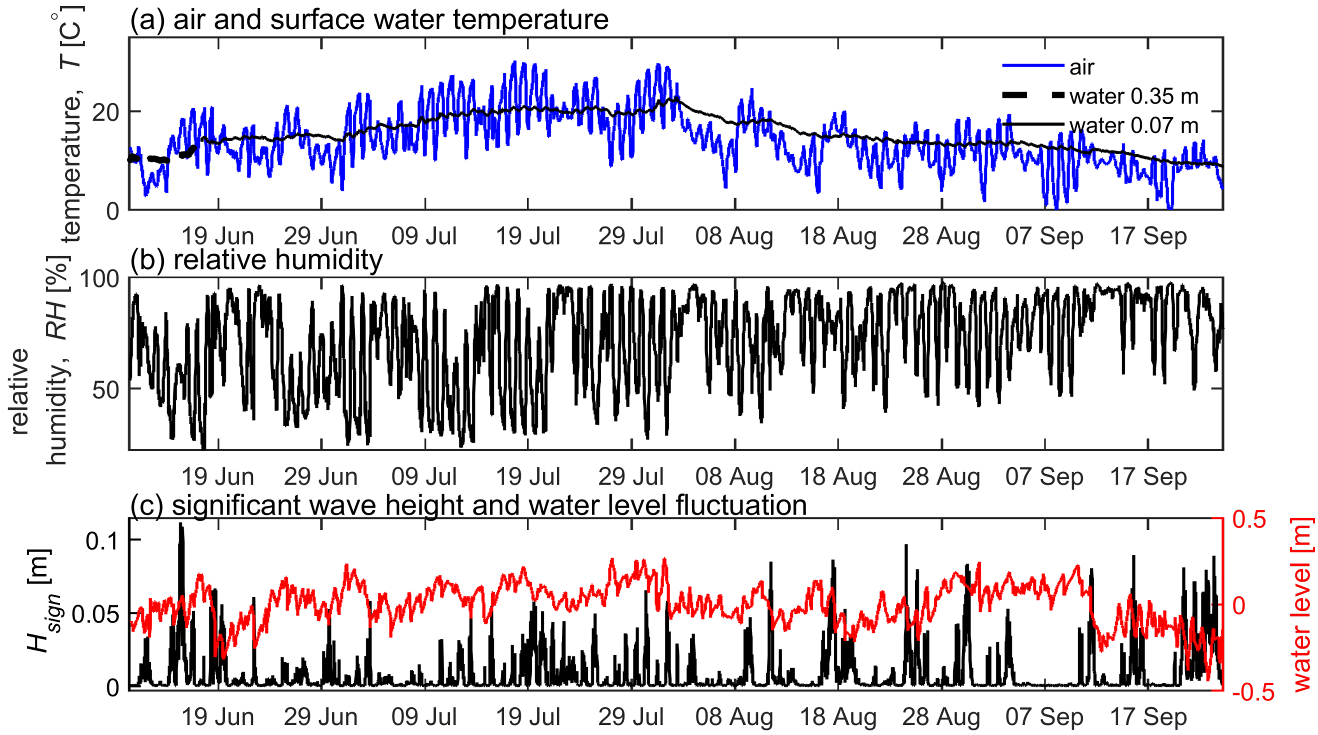

Figure S4. Time series of (a) air temperature (at 2 m height above the water, blue line) and surface water temperature (at 0.35 and 0.07 m depth, black line); (b) relative humidity. Significant wave height H_{sig} (black line) and water level fluctuations (red line). All data are shown as 10 min averages.

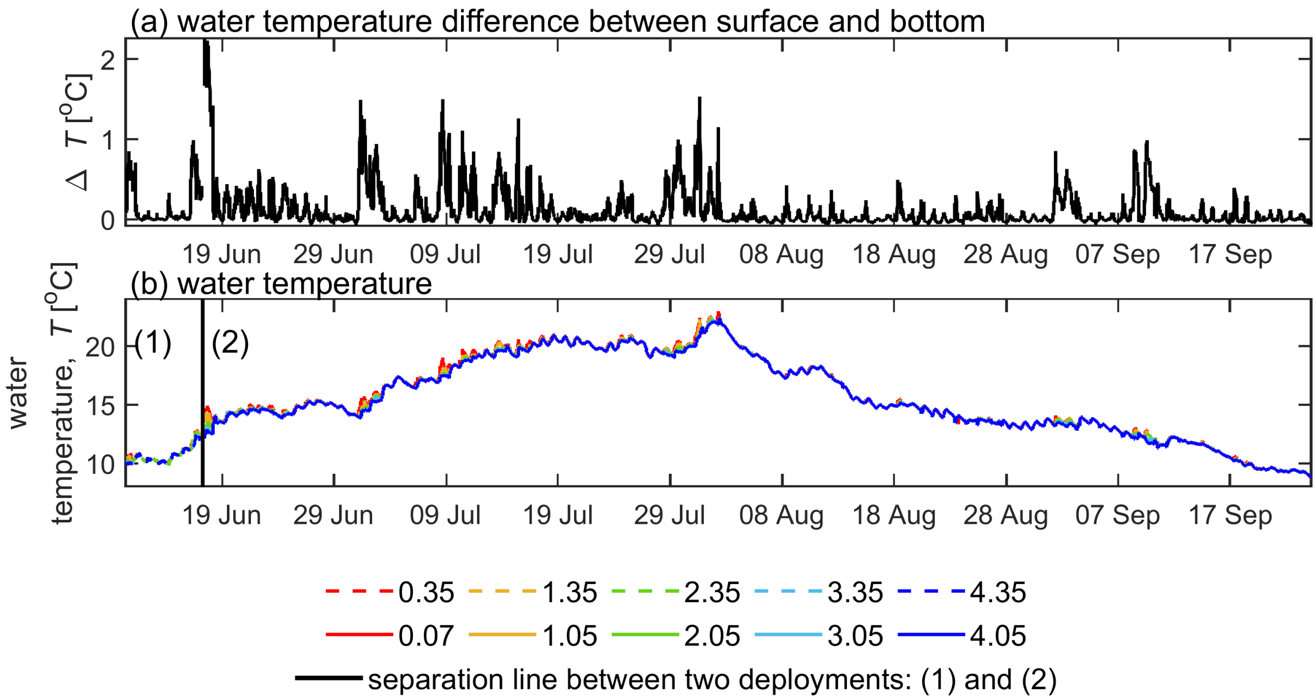

Figure S5. Time series of (a) water temperature difference between surface and bottom; (b) water temperature at different depths. The vertical black line separates two deployments periods of the thermistor chain: (1) 06.06 - 17.06 and (2) 17.06 - 24.09. All data are shown as 10 min averages.

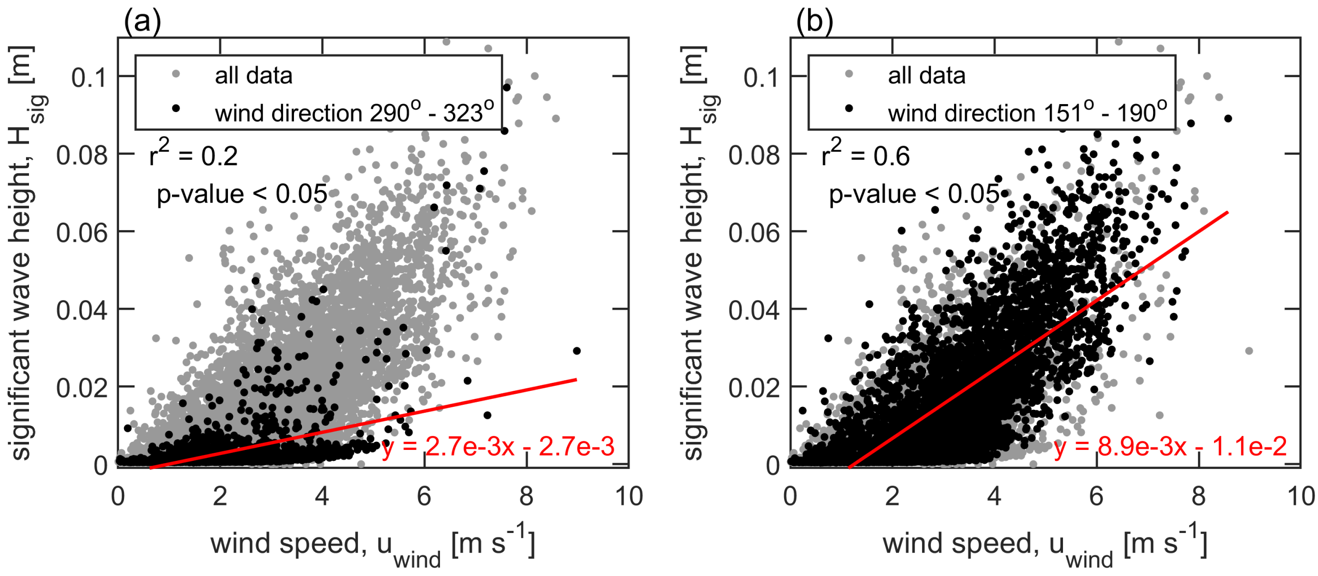

Figure S6. Significant wave height versus wind speed: (a) all data (light grey symbols) and data for which the wind direction was along aligned with the longitudinal flow velocity in the river channel ($290° \leqslant w_{dir} \leqslant 323°$, black symbols); (b) all data (grey symbols) and data for which the wind direction was against the river flow ($151° \leqslant w_{dir} \leqslant 190°$, black dots). The red lines show linear regressions (see legend), r^2 is a coefficient of determination, $p-$ value is the significance level for the slope coefficient different from zero in the linear regression model.

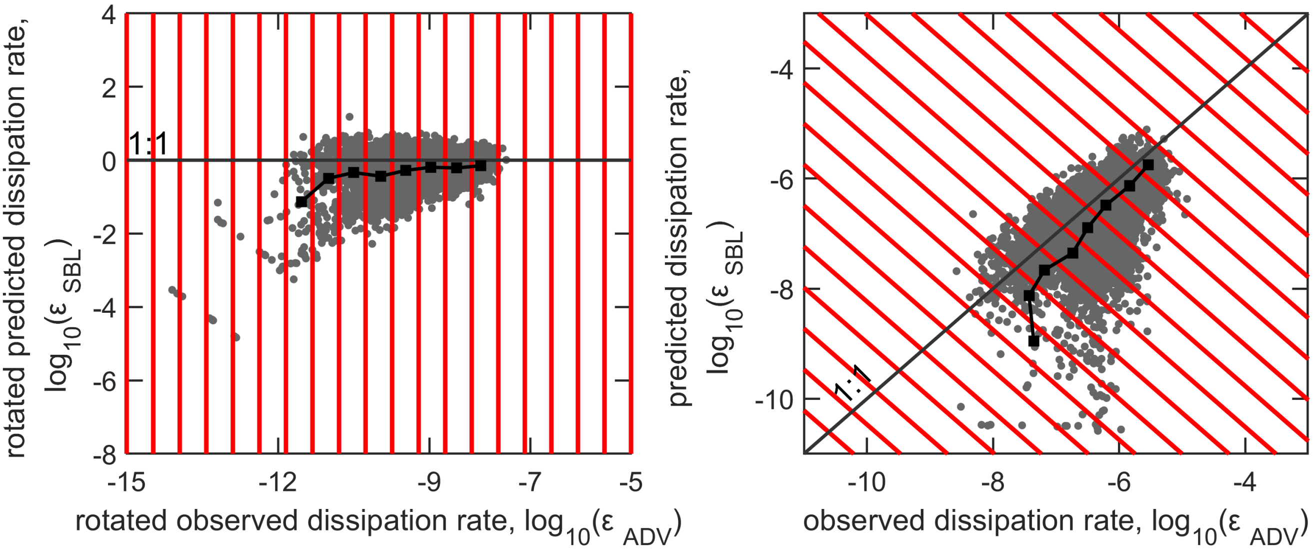

Figure S7. An example of logarithmic bin averaging of the data using measured ε_{ADV} and predicted ε_{SBL} dissipation rates from Sect. 3.2. Grey dots show: (a) rotated data (-45°); (b) original data. The solid dark grey line shows a 1:1 relationship, red lines indicate the selected intervals for averaging. The black line with square symbols shows the logarithmic bin average of the data.

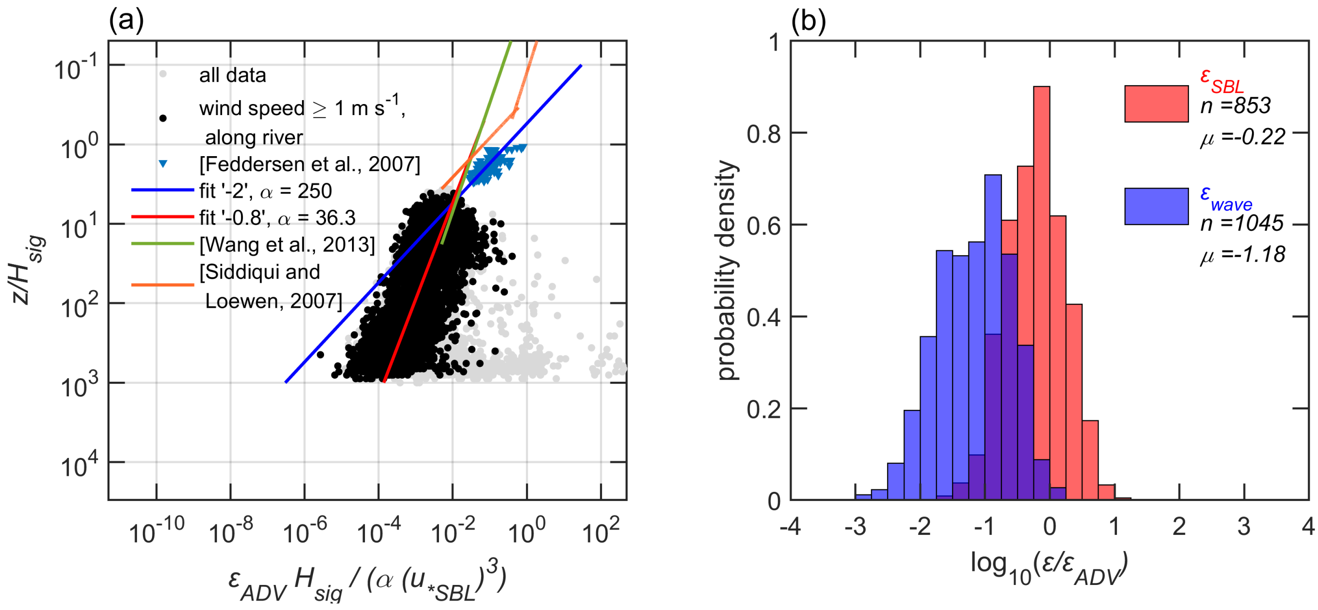

Figure S8. (a) Scaling of dissipation rate with surface waves. The x-axis shows a normalized dissipation rate (we used ε_{ADV}) and the y-axis is a wave-normalized depth (depth of the ADV measurements 0.4 m over significant wave height z/H_{sig}). Grey dots show all data, black dots highlight data for wind speed more than 1 m s^{-1} and for wind directions along the river; red line represents the fit to the data following Eq. A1 with the exponent $m = -0.8$ and the constant $\alpha = 36$ (Appendix A); blue triangles and blue line corresponds to the coastal ocean observations and its fit with the exponent $m = -2$ and the constant $\alpha = 250$ (Feddersen et al., 2007); green line represents the fit to the data obtained from a large lake with the exponent $m = -0.73$ (Wang et al., 2013); orange line shows scaling laws determined from a laboratory measurement (Siddiqui & Loewen, 2007). (b) Probability density distributions of the logarithmic ratio of predicted and observed dissipation rates. Predictions include estimates from bulk atmospheric forcing (ε_{SBL}, red color) and from wave-breaking scaling (ε_{wave}, blue color). The distributions were estimated for the selected data (black dots) in (a), but with the additional criterion of $H_{sig} > 2$ cm (empirically selected).

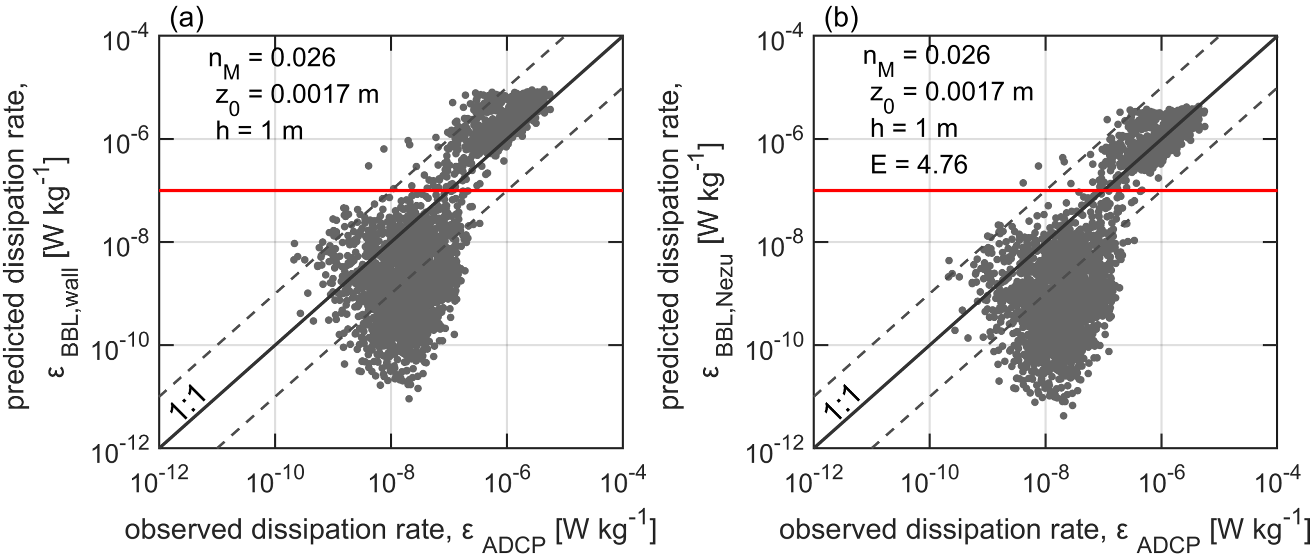

Figure S9. Bottom boundary layer scalings versus observed dissipation rate (grey points): (a) law of the wall; (b) Nezu approach. Red line shows the threshold value (10^{-7} W kg^{-1}). By assuming that the dissipation rates in the lower range were additionally affected by atmospheric forcing, we only considered dissipation rates exceeding this threshold in all subsequent analyses. n_M, z_0, h correspond to Manning's roughness coefficient, surface roughness at the sediment-water interface, the distance from the river bed, respectively. The solid grey line shows a 1:1 relation and two dashed lines indicate differences of one order of magnitude.

Table S1. Fitting parameters for the bottom boundary layer scaling (see Section 3.3). Different Manning's roughness coefficients (n_M) were used for law of the wall scaling in order to obtain the smallest error (R) between predicted $\varepsilon_{BBL,wall}$ and observed dissipation rates ε_{ADCP}. $n_M = 0.026$ s m$^{-1/3}$ corresponds to coarse sand (Chow, 1959; Arcement & Schneider, 1989). Corresponding roughness length and bottom drag coefficients are provided, the latter for a measurement height of the mean flow velocity at 1 m and at 3.8 m above the bed, respectively. 3.8 m corresponds to a water depth of 0.4 m, the sampling depth of the ADV.

Manning's roughness coefficient n_M [s m$^{-1/3}$]	Surface roughness length at the sediment-water interface z_0 [m]	Error R^a	Drag coefficient $C_{Dw,1m}$ [–]	Drag coefficient $C^b_{Dw,3.8m}$ [–]
0.026	0.0017	1.6749	0.0041	0.0028
0.0241	0.001	1.4581	0.0035	0.0025
0.023	0.00073	1.3716	0.0032	0.0023
0.0224	0.0006	1.3311	0.0031	0.0022
0.0219	0.0005	1.3011	0.0029	0.0021
0.0213	0.0004	1.2731	0.0027	0.002
0.0205	0.0003	1.2495	0.0026	0.0019
0.0195	0.0002	1.2365	0.0023	0.0017
0.0181	0.0001	1.2605	0.002	0.0015

[a] $R = 10^{\langle(\log_{10}\varepsilon_{wall} - \log_{10}\varepsilon_{ADCP})^2\rangle}$

[b] Corresponds to 0.4 m under the water surface.

Table S2. Fitting parameters for the bottom boundary layer scaling (see Section 3.3). Selected Manning's roughness coefficient ($n_M = 0.0195$ s m$^{-1/3}$) with the least error estimate from Table S1 was used for Nezu approach. Then the empirical constant E was varied in order to obtain the smallest error between predicted $\varepsilon_{BBL,Nezu}$ and observed dissipation rates $\varepsilon_{BBL,wall}$.

Manning's roughness coefficient n_M [s m$^{-1/3}$]	Surface roughness length at the sediment-water interface z_0 [m]	Empirical constant E [–]	Error R^a
0.026	0.0017	4.76^c	1.2394
0.0195	0.0002	4.76^c	1.5741
0.0195	0.0002	8.43^b	1.2528
0.0195	0.0002	9.8^c	1.2367
0.0195	0.0002	12^c	1.2537

[a] $R = 10^{\left\langle (\log_{10}\varepsilon_{Nezu} - \log_{10}\varepsilon_{ADCP})^2 \right\rangle}$

[b] The value was taken from (Tominaga & Sakaki, 2010).

[c] The value was taken from (Nezu, 1977).

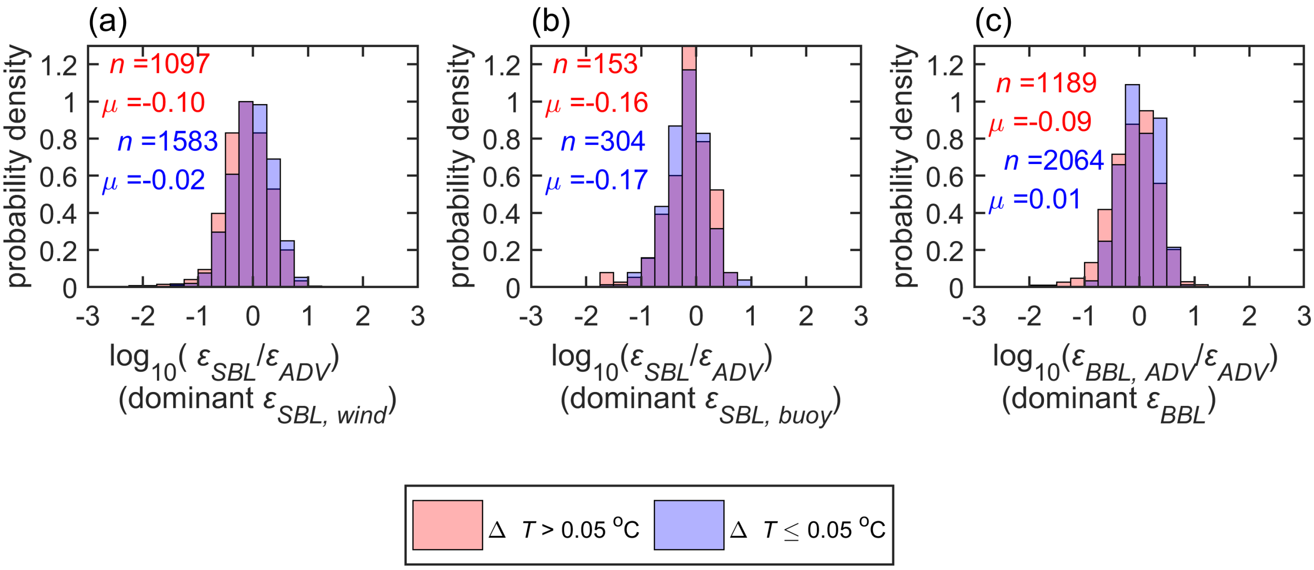

Figure S10. Probability density distributions of the ratio of predicted and observed dissipation rates when the water temperature difference between the surface and bottom (ΔT) large larger (red) or less (blue) than 0.05°C for the situations when: (a) wind; (b) buoyancy flux; (c) flow – was the dominant driver of the near-surface turbulence. The respective number of data points n and mean μ value of the logarithm of the ratio are shown the legend.

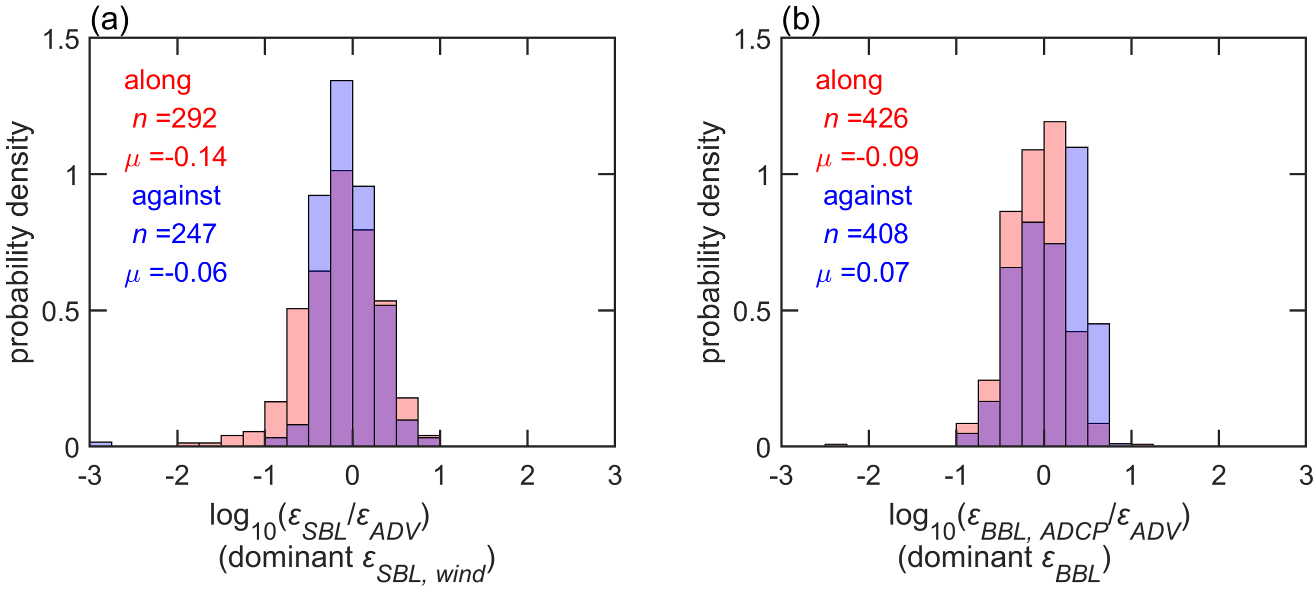

Figure S11. Probability density distributions of the ratio of predicted and observed dissipation rates for cases when wind was along the river flow ($290° \leqslant w_{dir} \leqslant 323°$, red) or against the flow ($151° \leqslant w_{dir} \leqslant 190°$, blue) for the situations when: (a) wind and (b) flow was the dominant driver of the near-surface turbulence. The respective number of data points n and mean μ value of the logarithm of the ratio are shown the legend.

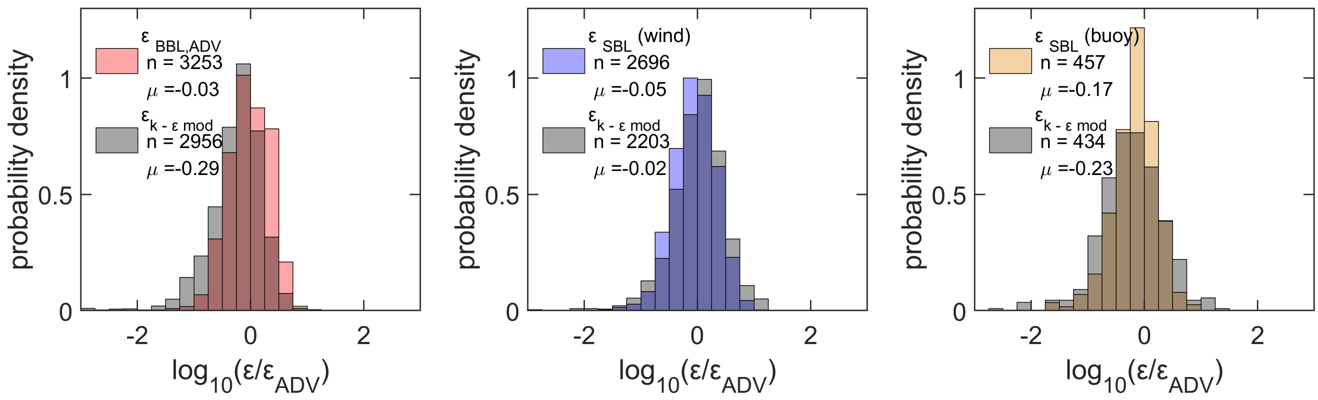

Figure S12. Probability density distributions of the logarithmic ratio of predicted and observed dissipation rates (ε_{ADV}) under different dominant forcing conditions for near-surface turbulence: (a) mean flow; (b) wind; (c) buoyancy flux. The predictions include the $k-\varepsilon$ model ($\varepsilon_{k-\varepsilon mod}$, grey color), bulk scaling using mean flow velocity ($\varepsilon_{BBL,ADV}$, red color), bulk scaling using mean wind speed (ε_{SBL}, blue color) and surface buoyancy flux (brown color). The respective number of data points n and mean μ value of the logarithm of the ratio are shown the legend.

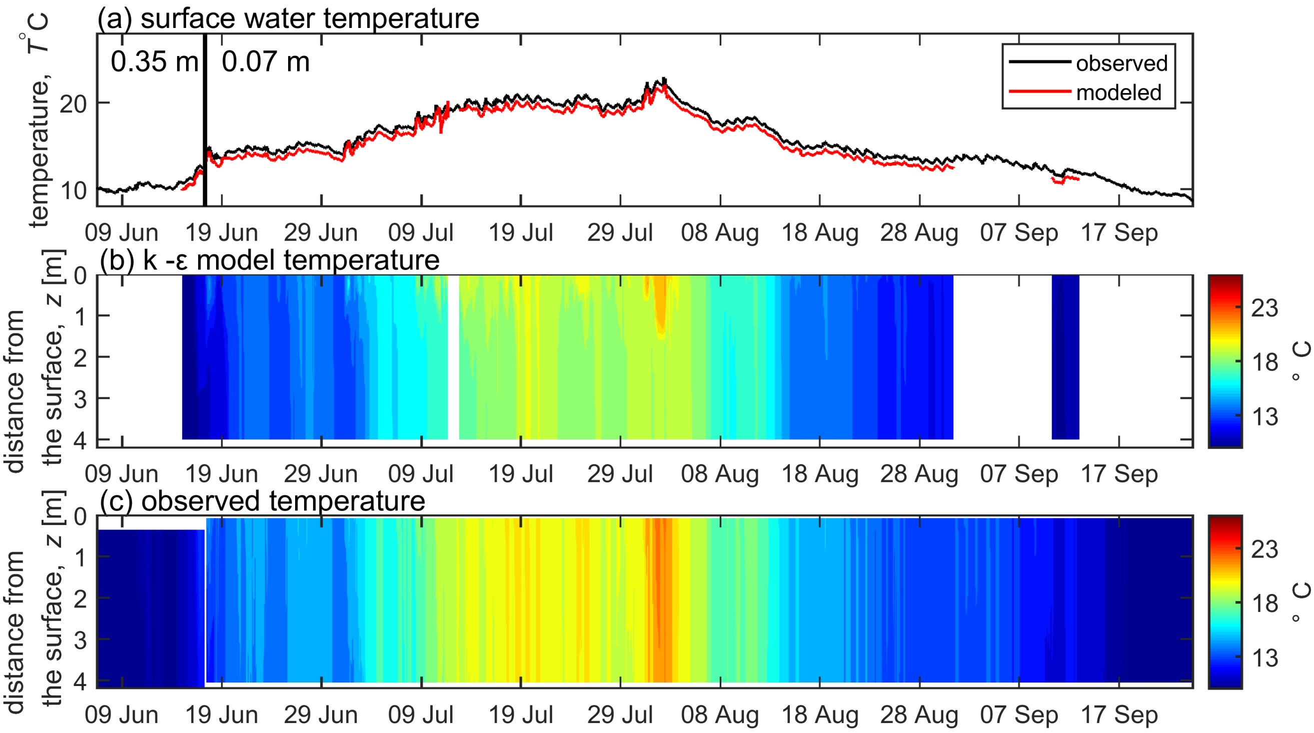

Figure S13. Time series of (a) surface water temperature: observed (black line) and modeled by $k - \varepsilon$ model (red line), vertical black line separates two deployments of the thermistor chain, numbers indicate water depth (0.35 m and 0.07 m), modeled temperature was interpolated; (b) modeled water temperature profiles; (c) observed water temperature profiles.

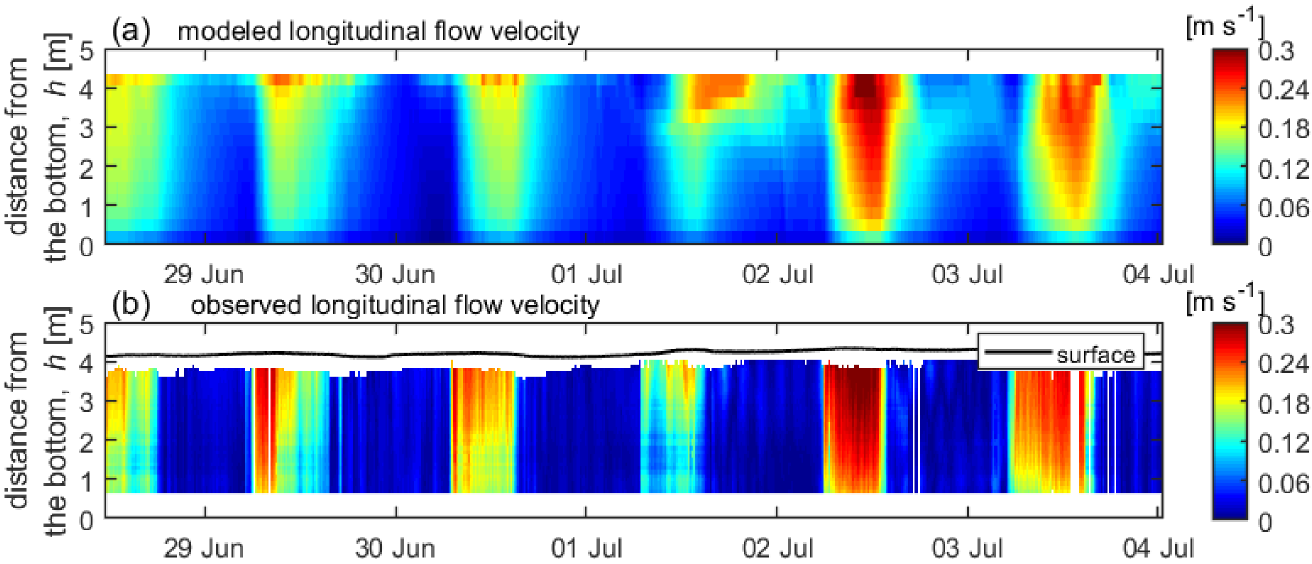

Figure S14. Time series of (a) modeled and (b) observed (ADCP) velocity profiles. Black line indicates the observed level of the water surface.